NASA-CR-173445
19840020197

OLD DOMINION UNIVERSITY RESEARCH FOUNDATION

DEPARTMENT OF GEOPHYSICAL SCIENCES
SCHOOL OF SCIENCES AND HEALTH PROFESSIONS
OLD DOMINION UNIVERSITY
NORFOLK, VIRGINIA

Technical Report No. GSTR-84-4

IDENTIFICATION OF AEROSOL COMPOSITION FROM MULTI-WAVELENGTH LIDAR MEASUREMENTS

By

Sidney Allen Wood

Technical Report

Prepared for the
National Aeronautics and Space Administration
Langley Research Center
Hampton, Virginia 23665

Under
Research Grant NCCI-28
Dr. Edward V. Browell, Technical Monitor
ASD - Chemistry & Dynamics Branch

(NASA-CR-173445) IDENTIFICATION OF AEROSOL COMPOSITION FROM MULTI-WAVELENGTH LIDAR MEASUREMENTS (Old Dominion Univ., Norfolk, Va.) 116 p HC A06/MF A01 CSCL 13B
N84-28266
Unclas
G3/45 00771

April 1984

N84-28266 #

DEPARTMENT OF GEOPHYSICAL SCIENCES
SCHOOL OF SCIENCES AND HEALTH PROFESSIONS
OLD DOMINION UNIVERSITY
NORFOLK, VIRGINIA

Technical Report No. GSTR-84-4

IDENTIFICATION OF AEROSOL COMPOSITION FROM MULTI-WAVELENGTH LIDAR MEASUREMENTS

By

Sidney Allen Wood

Technical Report

Prepared for the
National Aeronautics and Space Administration
Langley Research Center
Hampton, Virginia 23665

Under
Research Grant NCCI-28
Dr. Edward V. Browell, Technical Monitor
ASD - Chemistry & Dynamics Branch

Submitted by the
Old Dominion University Research Foundation
P.O. Box 6369
Norfolk, Virginia 23508

April 1984

ABSTRACT

IDENTIFICATION OF AEROSOL COMPOSITION FROM MULTI-WAVELENGTH LIDAR MEASUREMENTS

Sidney Allen Wood
Old Dominion University, 1983
Director: Dr. Scott T. Shipley

This paper seeks to develop the potential of lidar for the identification of the chemical composition of atmospheric aerosols. Available numerical computations suggest that aerosols can be identified by the wavelength dependence of aerosol optical properties. Since lidar can derive the volume backscatter coefficient as a function of wavelength, a multi-wavelength lidar system may be able to provide valuable information on the composition of aerosols. This research theoretically investigates the volume backscatter coefficients for the aerosol classes, sea-salts, and sulfates, as a function of wavelength. The results show that these aerosol compositions can be characterized and identified by their backscatter wavelength dependence. A method to utilize multi-wavelength lidar measurements to discriminate between compositionally different thin aerosol layers is discussed.

IDENTIFICATION OF AEROSOL
COMPOSITION FROM MULTI-
WAVELENGTH LIDAR MEASUREMENTS

by

Sidney Allen Wood
B.S. May 1980, Old Dominion University

A Thesis Submitted to the Faculty of
Old Dominion University in Partial Fulfillment of the
Requirements for the Degree of

MASTER OF SCIENCE

ATMOSPHERIC AND EARTH SCIENCE

OLD DOMINION UNIVERSITY
December 1983

Approved by:

Scott T Shipley
Scott T. Shipley
Director

Edward V Browell

ACKNOWLEDGEMENTS

I would like to express my appreciation to the faculty and students of the Geophysical Sciences Department of Old Dominion University for their support and friendship. I wish to extend special gratitude to Dr. Ron Welch, Dr. Robert Wilson, Dr. Cintia Piccolo and Vickie Conners for their encouragement and assistance while I was at Old Dominion. I would also like to express my thanks and affection to Linnea Svensson for many hours of support, advice and understanding.

I would like to thank the following employees of Systems and Applied Sciences Corporation for their help in computer software development and many useful inputs to my research: Dr. Syed Ismail, Tom Marshall and Barbara Gormsen. I want to especially thank Earl Thompson and Don Richardson for their assistance and advice while I was at NASA LaRC. They are truly computer experts.

I would like to express my deep gratitude to my thesis advisor, Dr. Scott Shipley, for his guidance and valuable criticisms during my progress at NASA. He stimulated my thoughts and helped develop my character and career. I also wish to thank Dr. Ed Browell for his

technical advice and insight into the physics of the UV-DIAL system. Dr. Browell provided both support and assistance throughout the course of my research.

Finally, to Dr. Earl C. Kindle, my graduate advisor at Old Dominion, a special thank you for the encouragement and guidance throughout my academic career. Dr. Kindle has been like a father to all of the meteorologists at Old Dominion and I shall always be in his debt.

This research was financially supported by the NASA contract NCCI-28.

TABLE OF CONTENTS

CHAPTER

LIST OF FIGURES

LIST OF TABLES

Tables

Page

I. INTRODUCTION

Lidar (laser radar) techniques have been developed over the last two decades for a wide range of studies of atmospheric properties (Russell, et al., 1981). This paper seeks to broaden these lidar capabilities to include the identification of the chemical composition of atmospheric aerosols. Available numerical computations suggest that broad classes of aerosols can be identified by the wavelength dependence of aerosol extinction and backscatter. Since backscatter signals can be obtained by lidar as a function of wavelength, a multi-wavelength lidar system may provide valuable information on the composition of atmospheric aerosols.

This thesis theoretically examines the wavelength dependence of volume backscatter coefficients for the tropospheric aerosol classes, sea-salts (NaCl) and sulfates ($[NH_4]_2SO_4$). Such a study must account for wavelength variations due to the natural variability of particle size distribution, refractive index, and relative humidity. The model analysis characterizes sea-salt and sulfate aerosol classes by demonstrating that the compositions are uniquely related to their backscatter spectral variations. The results support the idea of using compositional differences in a multi-wavelength lidar system to identify aerosol layers by their backscatter wavelength dependence. These results also provide useful information on the optimum lidar wavelengths for discrimination between the aerosol types considered.

Previous model calculations and experimental lidar measurements suggest that the wavelength dependence of the aerosol volume backscatter coefficient varies with aerosol chemical composition. The capabilities of multi-wavelength lidar for the identification of various aerosol composition from characteristic backscatter signatures has been explored, with moderate success, at infra-red wavelengths. The characteristic visible backscatter wavelength dependence expected for the aerosols in this study were established from previous pre-existing Mie model calculations.

Aerosol backscatter coefficients have been theoretically examined in the infra-red wavelength region 7.0 to 14.0 μm (Wright, 1980). Mie model calculations for basalt, H_2SO_4 (95%), H_2SO_4 (50%), ammonium sulfate $(NH_4)_2SO_4$, water and ice indicated significantly different backscatter features for each composition. Wright demonstrated that the six aerosol compositions were uniquely related by their infra-red backscatter spectral signatures. The author was also able to experimentally distinguish between high altitude ice clouds and low altitude water clouds with a multi-wavelength infra-red lidar system.

Mudd et al. (1982) investigated the potential of using a multi-wavelength lidar to differentiate between two sulfuric species in the stratosphere. Volume backscatter coefficients from ammonium sulfate and sulfuric acid particles were measured by a CO_2 laser under laboratory conditions, for the wavelength region 9.2 to 10.8 μm. Mie model calculations were made for comparison with the lidar measurements. The discrepancy between their experimental and theoretical values of volume backscatter coefficient wavelength dependence was suggested to be due to particle non-sphericity, inaccurate size distribution measurements or the presence of another species in the aerosol chamber. The author found that sulfuric acid and ammonium sulfate was distinguishable by backscatter signitures at infra-red wavelengths under laboratory conditions.

Available model calculations suggest that the broad aerosol classes, sea-salts and sulfates, can be identified by their backscatter wavelength dependence at visible wavelengths. Values of volume backscatter coefficients derived from the Mie calculations of Shettle and Fenn (1979), Dermendjian (1969), and Russell et al. (1981), indicate a wavelength dependence ranging from $\delta^{-2.0\pm0.32}$ for sulfates to $\delta^{-0.5\pm0.1}$ for sea-salts. These calculations were made for dry particles with one particle size distribution in the wavelength range 0.2 to 2.0 μm.

This study describes two tropospheric aerosol models and their optical properties. The models were based on a literature review of available data on aerosol physical properties such as particle size distribution (aerosol particle radius), complex refractive index (amount of scattering and absorption), and relative humidity. The optical properties of the aerosols were computed for the wavelength range 0.2 to 2.0 μm at various relative humidities ranging from 0 to 80 percent. The development of the two aerosol models and their physical properties is presented in Chapter II. The computation of backscatter coefficients from aerosol optical properties at the small size parameters 0 to 100 is discussed in Chapter III. Also included are the model calculations of backscatter wavelength dependence made for both sea-salts and sulfates. The discrimination between sea-salts and sulfates by backscatter wavelength dependence at various relative humidities is presented in Chapter IV. A method to retrieve the wavelength dependence of volume backscatter from a two wavelength lidar system is discussed in Chapter V.

II. MODELS OF AEROSOL PHYSICAL PROPERTIES

Atmospheric aerosol models have been developed to investigate optical properties of the maritime and continental classes of aerosols as a function of wavelength. Physical properties (i.e., particle size distribution, refractive index, relative humidity) for both of these aerosol types can vary significantly in the atmosphere, consequently influencing the particle's optical properties. The aerosol physical properties used in the models are based upon measurements taken from the literature for various geographical locations, and seasons of the year. The measured range of natural variations found in both aerosol size distributions were incorporated into these models. Also included were the effects of increasing and decreasing relative humidity variations on aerosol particle growth and refractive indices. The models for sulfate and sea-salt aerosols are presented in a way which attempts to account for natural variations in the particle size distribution, refractive index, and relative humidity.

2.1 MODEL SIZE DISTRIBUTIONS

The aerosol size distributions used in the continental and maritime models were based upon available experimental measurements, to provide a range of natural variability. Sulfate and sea-salt size distributions were collected from the literature for both airborne and surface locations, under various meteorological conditions. Some relevant information (i.e., location, collection method and efficiency, meteorology, time of year) on the size distributions is presented in Table 1a for sea-salts, and Table 1b for sulfates. A normalization of the distribution curves revealed a significant size distribution variation in the small and large particle radius sizes as shown in Figs. 1a and 1b. This natural variability of the particle size distributions was incorporated into the two aerosol models.

A non-linear regression routine was used to best fit each empirically derived particle size distribution to a log normal curve.

$$\frac{dN(r)}{dr} = \left(\frac{1}{\ln(10)\, r\sigma_i\sqrt{2\pi}}\right) \mathrm{EXP}\left\{-\frac{(\log r - \log r_i)^2}{2\sigma^2}\right\} \qquad (1)$$

where

$N(r)$	is the total concentration of aerosol particles with radii greater than r,
$\frac{dN(r)}{dr}$	is the number of particles (cm^{-3}), with radii between r(μm) and $r+dr$,
r_i	is the mode radius,

Table 1a. Data on collected maritime (sea-salt) particle size distributions.

Size Distribution	Location	Meteorology	Collection Method Efficiency	Time	Source
1	Cape Blanco	High pressure ridge across southern Oregon. Surface winds from southwest representing a pacific air mass with no anthropogenic contamination.	Royco P C 200A photometric particle counter, air filters, Goetz aerosol centrifuge. The Royco measured a particle radius range of $0.15<r<4\ \mu m$. For particles greater than $1.0\ \mu m$, the instrument was inaccurate.	NOV 6, 1969 910-1530 Alt: 2200m	Junge, 1969
2	Cape Blanco	High pressure ridge across southern Oregon. Surface winds from southwest representing a pacific air mass with no anthropogenic contamination.	Royco P C 200A photometric particle counter, air filters, Goetz aerosol centrifuge. The Royco measured a particle radius range of $0.15 < r < 4\ \mu m$. For particles greater than $1.0\ \mu m$, the instrument was inaccurate.	SEP 28, 1969 800-1700 Alt: 200m	Junge, 1969
3	Crater Lake	Quasi-stationary High over eastern Oregon representing a pacific air mass.	Royco P C 200A photometric particle counter, air filters, Goetz aerosol centrifuge. The Royco measured a particle radius range of $0.15 < r < 4\ \mu m$. For particles greater than $1.0\ \mu m$, the instrument was inaccurate.	SEP 28, 1969 800-1700 Alt: 200m	Junge, 1969
4	Remote Area of Pacific Ocean	Relative humidity less than 50%.	Two single optical counters, Nuclepore polycarbonate filter. A combination of active scattering spectrometer and classical scattering probe was used for particles $0.15 < r < 0.75\ \mu m$. A forward scatter spectrometer probe was used for particles $0.25 < r < 3.0\ \mu m$. The filters were 100% efficient for radius $> .5\ \mu m$.	1980 Alt: 5-6km	Patterson et al, 1980 (log normal fit)

Table 1a. continued.

5	West Coast of Ireland	Relative humidity was 0%	Cascade impactor. The efficiency of the impactor was low for the smaller particles ($< 0.5\mu m$).	Summer 1958	Metnicks 1958
6	Atlantic Ocean of $0<\phi<20°S$	Temperature: 6.5°C Humidity: 78% Wind Speed: 12 m/s	Membrane filter, particle counter was used for the radius range $0.03<r<25\mu m$. For radius 0.03 m, the collection efficiency was 70%.	Summer 1971-1972	Meszaros 1974
7	Atlantic Ocean of $40<\phi<60°S$	Temperature: 24°C Humidity: 71% Wind Speed: 6 m/s	Membrane filter, particle counter was used for the radius range $0.03<r<25\mu m$. For radius $0.03\mu m$, the collection efficiency was 70%.	Summer 1971-1972	Meszaros 1974
8	Atlantic Ocean of $\phi>60°$	Temperature: 0.8°C Humidity: 85% Wind Speed: 7 m/s	Membrane filter, particle counter was used for the radius range $0.03<r<25\mu m$. For radius $0.03\mu m$, the collection efficiency was 70%.	Summer 1971-1972	Meszaros 1974

Table 1b. Data on collected continental (sulfate) particle size distributions.

Size Distribution	Location	Meteorology	Collection Method and Efficiency	Time/ Altitude	Source
1	Soesterberg	Cool, dry continental polar air mass. Northeasterly winds. Relative humidity was 85-90%.	Royco single particle counter. Collection efficiency was satisfactory for $0.4 < r < 14$ μm.	APR 12, 1976 1226 GMT Alt: 1500m	Cress, 1980
2	Soesterberg	Cool, dry continental polar air mass. Northeasterly winds. Relative humidity was 85-90%.	Royco single particle counter. Collection efficiency was satisfactory for $0.4 < r < 14$ μm.	APR 12, 1976 1246 GMT Alt: 3000m	Cress, 1980
3	Meppen	Old maritime air mass modified to be strongly continental. Southwesterly winds. Relative humidity was 50%.	Royco single particle counter. Collection efficiency was satisfactory for $0.4 < r < 14$ μm.	AUG 5, 1977 Alt: 1011m	Cress, 1980
4	Meppen	Old maritime air mass modified to be strongly continental. Southwesterly winds. Relative humidity was 50%.	Royco single particle counter. Collection efficiency was satisfactory for $0.4 < r < 14$ μm.	AUG 5, 1977 947 GMT Alt: 3060m	Cress, 1980
5	Komlosi Telep	Weather was not given since the distribution was averaged over the season.	Czechoslavakian membrane filter 1.7m above ground facing wind direction. Counted and sized particles in the radius range 0.02-0.5μm. A phase contrast optical microscope was used for particles 0.5-100μm. The collection efficiency was 60% for 0.05μm.	Summer 1974-1976 Alt: 1300m	Meszaros, 1978

Table 1b. continued.

6	Komlosi Telep	Weather was not given since the distribution was averaged over the season.	Czechoslavakian membrane filter 1.7m above ground facing wind direction. Counted and sized particles in the radius range 0.02-0.5μm. A phase contrast optical microscope was used for particles 0.5-100μm. The collection efficiency was 60% for 0.05 m.	Winter 1974-1976 Alt: 1300m	Meszaros, 1978
7	Komlosi Telep	Weather was not given since the distribution was averaged over the season.	Czechoslavakian membrane filter 1.7m above ground facing wind direction. Counted and sized particles in the radius range 0.02-0.5μm. A phase contrast optical microscope was used for particles 0.5-100μm. The collection efficiency was 60% for r > 0.05μm.	Summer 1974-1976 Alt: 1300m	Meszaros, 1978
8	N/A*	N/A	Log normal curve fit to Whitby and Cantrell (1976). Typical range of values for the accumulation aerosol mode	Distribution good for altitudes 200m	Shettle & Fenn 1979

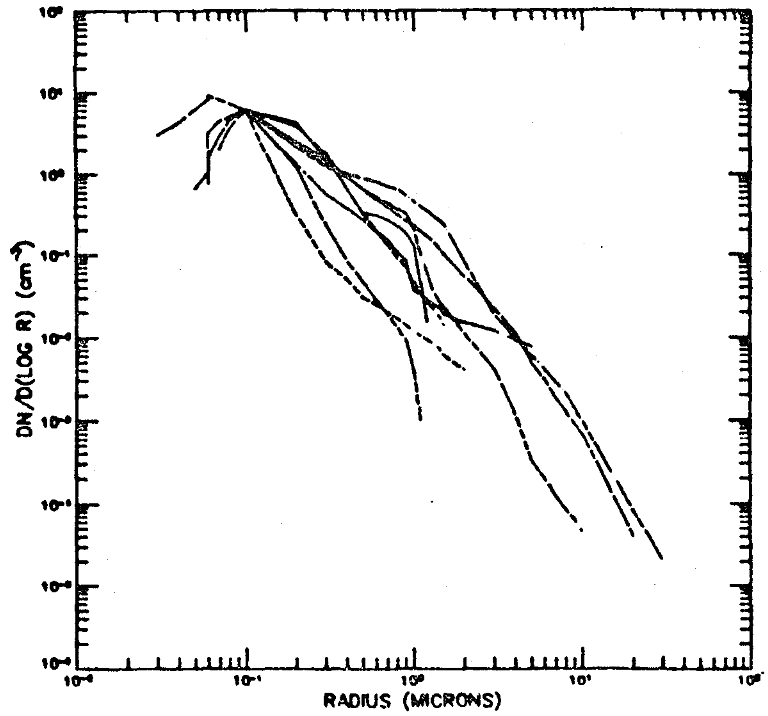

Fig. 1a. Eight maritime particle size distributions collected from available literature. The distributions were normalized to 6 cm^{-3} for $r=0.1\mu m$ to show relative variability of the particle size distributions.

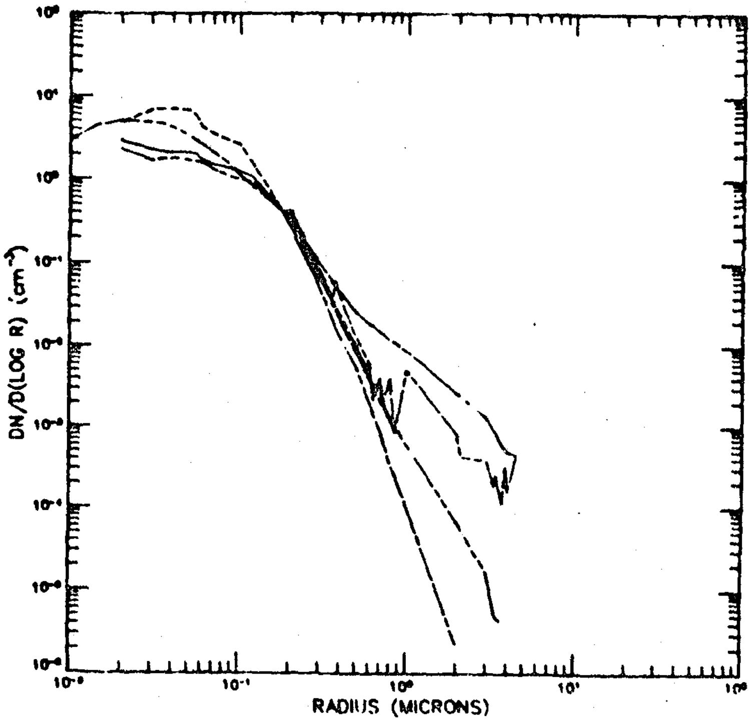

Fig. 1b. Eight continental particle size distributions collected from available literature. The distributions were normalized to 4 cm^{-3} for $r=0.1\,\mu m$ to show relative variability for the particle size distributions.

σ_i is the mode standard deviation.

The use of a log normal curve to represent particle size distributions has been discussed in the literature (Whitby et al., 1972; Kelkar and Joshi, 1975; Thomalla and Quenzel, 1982; Patterson et al., 1980). A comparison between a particle size distribution taken from Junge (1969) and the log normal curve used in the model to approximate the distribution is presented in Fig. 2. The general slope of the Junge distribution is shown to be adequately simulated by a log normal curve even though there are some discrepancies between the two curves, especially at the larger radii. The values of the mode radius and mode standard deviation that best fit the distributions are shown in Table 2a for sea-salts, and Table 2b for sulfates.

Table 2a. Sea-salt

SD	r_i	σ_i
1	0.06	0.40
2	0.10	0.37
3	0.10	0.33
4	0.28	0.21
5	0.24	0.25
6	0.32	0.39
7	0.26	0.44
8	0.16	0.40
$\bar{r}_i$	0.190	
$\bar{\sigma}_i$	0.360	
σ_{r_i}	0.093	
σ_{σ_i}	0.092	

Table 2b. Sulfates

SD	r_i	σ_i
1	0.07	0.31
2	0.05	0.35
3	0.05	0.36
4	0.07	0.38
5	0.07	0.17
6	0.09	0.21
7	0.07	0.26
8	0.07	0.26
$\bar{r}_i$	0.0675	
$\bar{\sigma}_i$	0.2875	
σ_{r_i}	0.0128	
σ_{σ_i}	0.0750	

ORIGINAL PAGE IS
OF POOR QUALITY

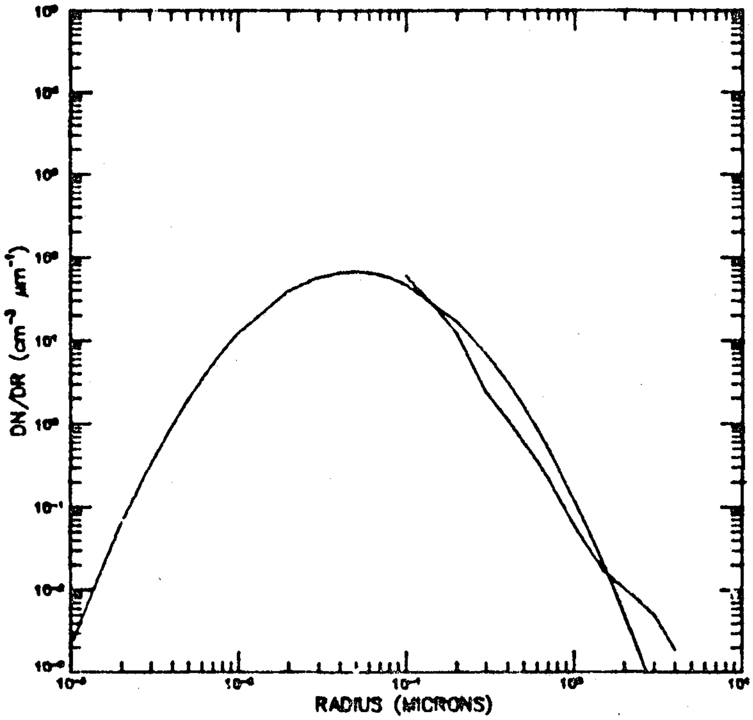

Fig. 2. A log normal size distribution best fit to a Junge, 1969 particle size distribution.

The means and standard deviations of the log normal mode parameters (also shown in Tables 2a and 2b) were used with a random data generator to produce synthetic particle size distributions. The parameters r_i and σ_i were assumed to be normally distributed with variances as shown in Tables 2a and 2b. The randomly generated parameters which define the particle size distributions are presented in Table 3.

Table 3. Mode Parameters for Synthetic Particle Size Distributions.

SIZE DISTRIBUTION	MARITIME (OCEANIC)		CONTINENTAL (RURAL)	
	r_i	σ_i	r_i	σ_i
1	.355	.470	.0835	.374
2	.163	.295	.0863	.231
3	.340	.383	.0838	.303
4	.112	.352	.0579	.278
5	.146	.364	.0638	.287
6	.218	.442	.0727	.352
7	.190	.351	.0697	.277
8	.170	.376	.0674	.298
9	.175	.413	.0679	.327
10	.162	.365	.0662	.289
11	.195	.310	.0783	.243
12	.147	.408	.0648	.323
13	.159	.328	.0689	.258
14	.246	.253	.0754	.197
15	.114	.398	.0583	.315
16	.149	.505	.0644	.403
17	.340	.284	.0813	.222
18	.201	.337	.0710	.266
19	.250	.385	.0758	.305
20	.196	.343	.0704	.271
21	.173	.353	.0676	.279
22	.251	.394	.0758	.312
23	.156	.304	.0663	.141
24	.175	.362	.0654	.238
25	.270	.359	.0679	.286

Since this study is mainly concerned with free tropospheric aerosol particles, only one mode (accumulation mode) was used for each distribution, even though size distributions of aerosol particles have been documented as having a multi-mode structure (Whitby et al., 1972; Willeke and Whitby, 1975; Willeke, 1974). The use of only one mode for the particle size distribution at the higher altitudes is consistent with the results of Whitby and Cantrell (1975).

2.2 THE EFFECTS OF INCREASING AND DECREASING RELATIVE HUMIDITY ON AEROSOL PROPERTIES

In this section, the effects of humidity variation on aerosol properties and how they are incorporated into the models is discussed. As relative humidity increases, aerosol particles in the atmosphere tend to grow as water vapor condenses onto the particle by the process of adsorption (Fitzgerald, 1975). The process will continue until at some critical relative humidity, the particle will undergo a sudden change to a saturated solution droplet by the process of absorption (Fitzgerald, 1975; Covert, Charlson, and Ahlquist, 1972). The process of particle water uptake not only increases the size of the particle, but also changes the aerosol chemical composition, and therefore the refractive index.

Numerous authors have addressed the problem of atmospheric particle growth as a function of relative humidity (Orr et al., 1958; Winkler and Junge, 1971 and

1972; Meszaros, 1971; Herbert, 1975; Fitzgerald, 1975; Tang, 1976; Tang et al., 1977a, 1977b and 1978; Thudium, 1978; Fitzgerald et al., 1982), and the foremost of the studies is the work of Hanel (1968, 1970, 1971, 1972a, 1976, 1979, 1980). Hanel constructed equilibrium growth curves of "typical" aerosol particles based on the characteristic behavior of aerosol group samples.

A semi-empirical model has been developed by Hanel to describe the growth of a particle's radius due to relative humidity. In order to derive the equilibrium growth of a particle, the water activity (i.e., the equilibrium relative humidity over a plane surface) of the solution must be measured (Hanel, 1976). Hanel made the approximation that the volume (V) of a solution drop was equal to the size of the volume of the dry spherical particle $V_o = \frac{4}{3}\pi r_o^3$, plus the volume of pure water $V_\omega = \frac{4}{3}\pi r_\omega^3$ condensed on it

$$\frac{V}{V_o} = 1 + \frac{\rho_o}{\rho_\omega}\left(\frac{M_\omega}{M_o}\right) \qquad (2)$$

The equivalent radius of a particle, the radius of a sphere with the same volume as the solution drop, can then be defined as

$$r = r_o\left(1 + \frac{\rho_o}{\rho_\omega}\left(\frac{M_\omega}{M_o}\right)\right)^{1/3} \qquad (3)$$

where

r	is the equivalent radius,
r_0	is the equivalent radius at a relative humidity of zero
ρ_0	is the mean bulk density of the particle at RH=0,
ρ_w	is the density of water,
M_w	is the mass of water condensed on the particle,
M_0	is the mass of the particle in its dry state.

The particle equivalent radius is reliable for calculating the humidity dependence on extinction and scattering coefficients even at low relative humidities(Hanel, 1976).

According to the refractive index measurements of Volz (1972, 1973), the amount of absorption of continental and oceanic type aerosols is quite low when compared with the amount of scattering at the visible wavelengths, therefore only the real part of the complex refractive index was used in this study. The effective refractive index, m, can be easily calculated once the "wet" particle radius has been found by the mass weighted function by the equation

$$m = m_w + (m_0 - m_w)\left(\frac{r_0}{r(rh)}\right)^3 \qquad \text{(Hanel, 1976)} \qquad (4)$$

where

m_w is the real component of the complex refractive index for water,

m_o is the real component of the complex refractive index for the dry substance.

The refractive indices for water as a function of wavelength were taken from the measurements of Hale and Querry (1973), and are shown in Table 4. Also shown are the dry refractive indices for the maritime and continental models taken from Shettle and Fenn (1979), which are based on the measurements of Volz (1972, 1972, 1973).

Table 4. Refractive index of water, sea-salt, and sulfate.

WAVELENGTH (μm)	HALE & QUERRY (1973) WATER	VOLZ(1972) SEA-SALT	VOLZ(1973) SULFATE
0.30	1.35	1.51	1.53
0.40	1.34	1.50	1.53
0.55	1.33	1.50	1.53
0.70	1.33	1.49	1.53
0.90	1.33	1.48	1.52
1.05	1.33	1.47	1.52
1.35	1.32	1.47	1.51
1.50	1.32	1.46	1.51
1.90	1.31	1.45	1.46
2.00	1.31	1.45	1.42

The use of Hanel's equations to describe the relative humidity effects on "typical" aerosol particles requires measurements of the mass ratio between dry substances and water, relative humidity, and the dry particle density. Such measurements have been made for maritime, industrial, continental, and desert type aerosols by Hanel (1976) and Hanel and Lehmann (1980). Their data was collected for aerosol particles exposed to increasing and decreasing relative humidity conditions. For decreasing relative humidity, a deliquescent material will contain more water than the particle would under increasing relative humidity. This result is called the hysteresis effect and is mainly due to the phenomenon that evaporating salt solutions tend to supersaturate with respect to the salt in the solution. The hysteresis curves for maritime type aerosols have been found to be broader at higher relative humidities than continental type aerosols (Hanel and Lehmann, 1980), as shown in Fig. 3. These results suggest that maritime aerosol type particles can return to their original size at lower relative humidities, whereas the continental type particles do not.

2.3 MARITIME (OCEANIC) AEROSOL MODEL

The composition for the maritime aerosol model is assumed to be pure sea-salt. Aerosol compositions throughout the marine boundary layer (MBL) and marine free troposphere (MFT) have been documented as being composed

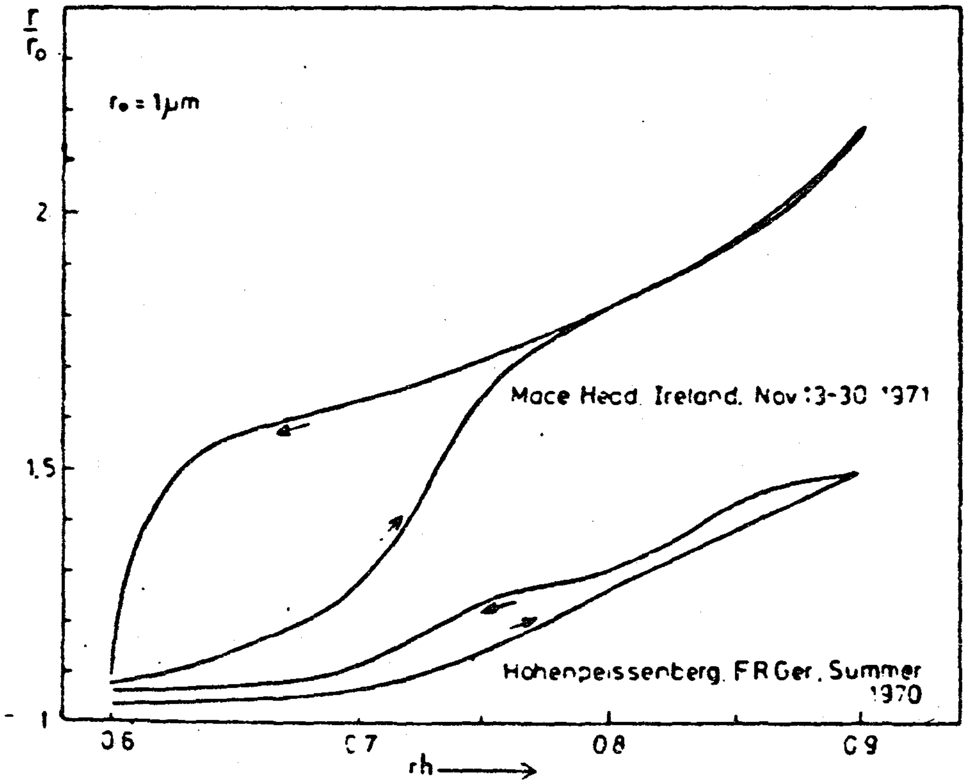

Fig. 3. Hysteresis curves for maritime aerosols (Mace, Ireland) and continental aerosols (Hohenpeissenberg, Germany) (Hanel and Lehmann, 1980).

of a mixture of oceanic aerosols and continental background aerosols (Junge, 1969; Meszaros and Vissy, 1974; Patterson et al., 1980). According to Meszaros and Vissy, the larger particles consist mainly of sea-salt, while the smaller particles are the rural background aerosols. Particle size distribution measurements (Patterson et al., 1980) show that the larger sea-salt particles in the MBL predominate over the sea-salt particles found in the MFT.

According to Blanchard and Woodcock (1980), sea-salt particles are created during the evaporation of sea water drops, and can grow to larger particle sizes due to absorption of water under high relative humidity conditions. The vertical distribution of sea-salt particles was measured by Blanchard and Woodcock (1980) for various wind speeds. The presence of the smaller sea-salt particles were found throughout the lower free troposphere (i.e., 0.5-2.0 km), and at altitudes of approximately 0.5 to 0.6 km, a sea-salt particle inversion was measured.

The refractive indices for the sea-salt aerosols are based on the measurements of Volz (1972). They are presented as a function of wavelength in Table 4.

The particle size distribution for the maritime aerosol model is a single mode log normal curve. The log normal mode parameters, r_i and σ_i, of the distribution were randomly varied based on real size distribution measurements as explained in section 2.1. The mode parameters defining the particle size distributions used in the model are presented in Table 3. A normalization of the log normal distributions to 1.08 $cm^{-3} \mu m^{-1}$ for a radius of 0.1 μm is shown in Fig. 4, thus depicting the natural variation in relative number concentration one might expect for maritime particle size distribution.

The incorporation of relative humidity effects on dry sea-salt particle radius is based on Hanel and Lehmann's (1980) mass ratio measurements for sea-salt particles and water. The mass ratio measurements are shown in Table 5, for increasing and decreasing relative humidities. Also shown in the table is the dry particle density and threshold water activity, the water activity needed for a particle to be completely covered by water.

Table 5. Mass ratio measurements for sea-salt and water for increasing and decreasing relative humidity. The dry particle density ρ and threshold water activity A_{wt} are also included (Hanel and Lehmann, 1980).

MASS RATIO ($H_2O/NaCl$)

rh	Increasing	Decreasing
20	0.0016	0.0019
30	0.0169	0.0166
40	0.0380	0.0392
50	0.0676	0.0884
60	0.1390	0.1740
65	0.2900	1.5500
70	0.6600	1.8100
75	2.2000	2.1900
80	2.5800	2.6800
A_{wt}	0.7000	0.6490
ρ (gm/cm^{-3}) 1.93		

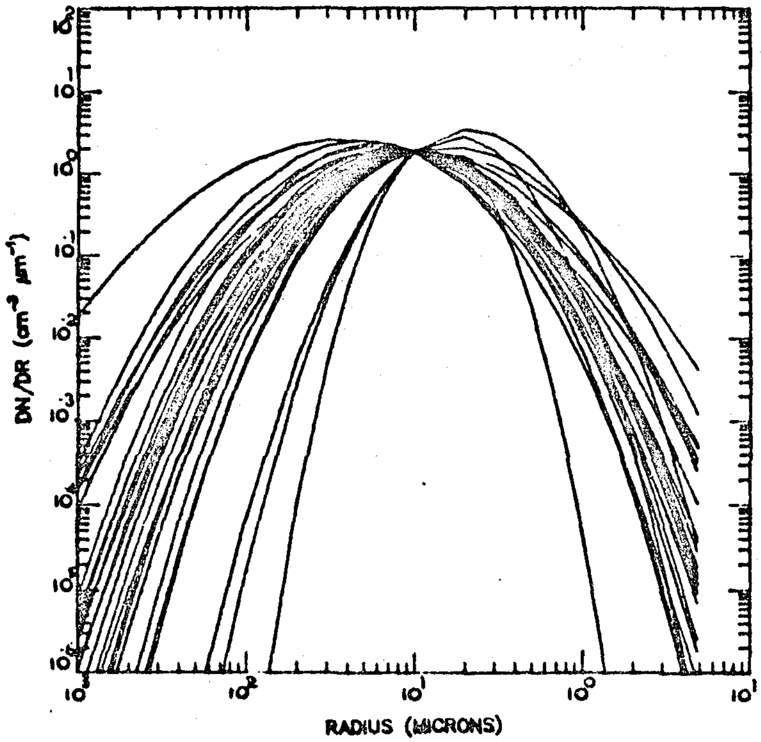

Fig. 4. Twenty-five log normal particle size distributions for the maritime (oceanic) aerosol model. All size distributions are normalized to 1.08 cm^{-3} μm^{-1} for r=0.1 μm to show relative variability of the particle size distributions.

The effects of increasing relative humidity on a maritime particle size distribution is shown in Fig. 5 for the relative humidities 0, 60, 70, and 80%. As explained in section 2.2, the relative humidity effects on particle size is minimal at lower relative humidities. As relative humidity increases and reaches the critical relative humidity for sea-salt aerosols, the particle size distribution exhibits a significant shift towards the larger particle sizes. For decreasing relative humidity (from near 100%), Fig. 6 demonstrates the deliquescent nature of sea-salt particles for the relative humidities 80, 70, 60, and 0%.

2.4 CONTINENTAL (RURAL) AEROSOL MODEL

The continental (rural) aerosol differs greatly in source, size, and composition from oceanic type aerosols. Usually, the tropospheric rural aerosols are considered to be background sulfate particles with little or no anthropogenic influences. For this study, the composition of the sulfate particles were assumed to be ammonium sulfate ($(NH_4)_2SO_4$), which is the principle constituent of the background sulfate species (Volz, 1972; Junge, 1953).

The refractive indices used for the model were based on the measurements of Volz (1972, 1973), and are presented as a function of wavelength in Table 4.

As in the maritime model, a single mode log normal curve is used to represent the particle size distribution.

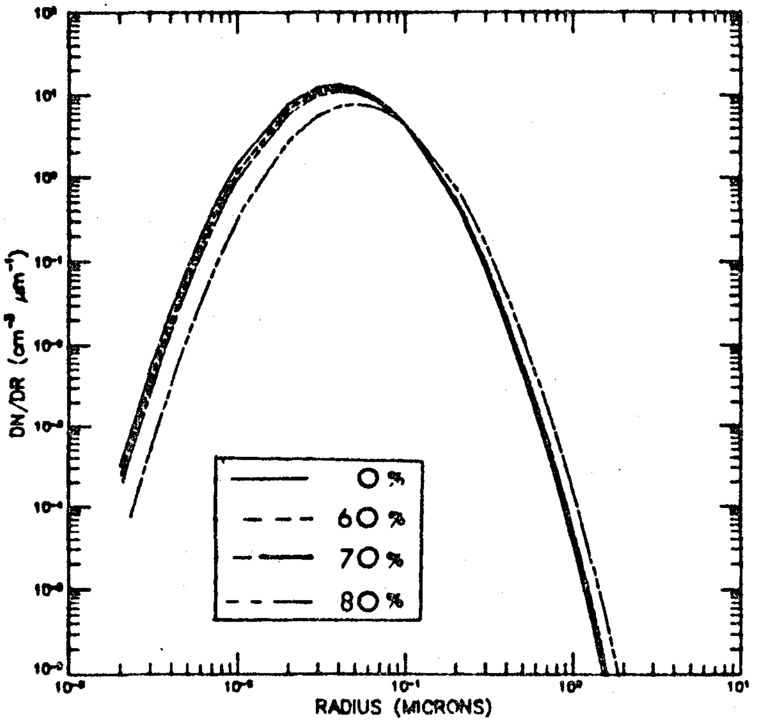

Fig. 5. Maritime modeled log normal particle size distribution for the increasing relative humidities 0, 60, 70, and 80%. The curves are normalized to 4 $cm^{-3} \mu m^{-1}$ for $r=0.1 \mu m$.

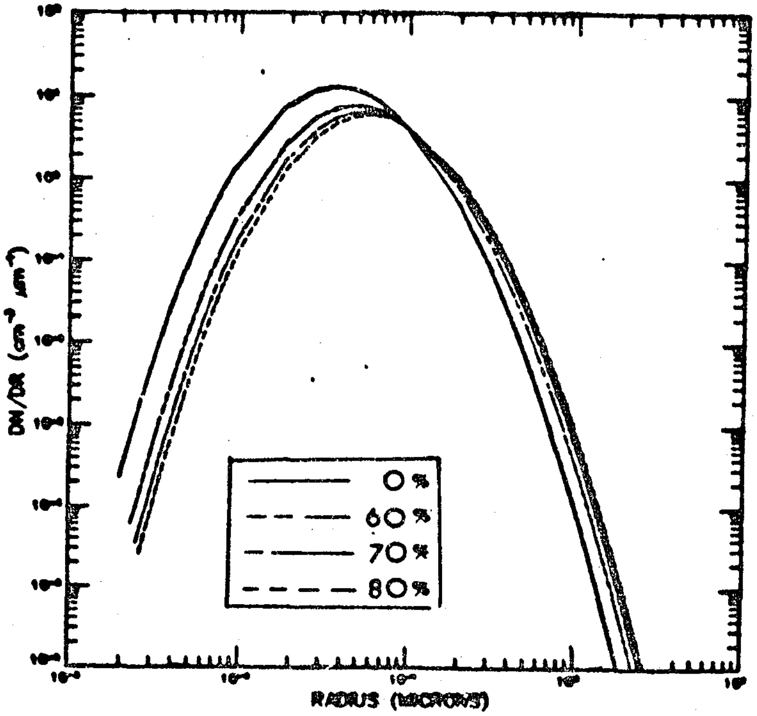

Fig. 6. Maritime modeled log normal particle size distributions for the decreasing relative humidites 80, 70, 60, and 0%. The curves are normalized to 4 $cm^{-3}\mu m^{-1}$ for $r=0.1\mu m$.

The log mode parameters, r_i and σ_i, were randomly varied based on real measurements of the continental size distribution and are presented in Table 2. The range of expected natural variation for the continental size distributions is shown in Fig. 7, where the log normal distribution curves have been normalized to 4.9 cm^{-1} μm^{-1} for a radius of 0.1 μm.

Mass ratio measurements of ammonium sulfate and water made by Hanel and Lehmann (1980) were used to include the effects of relative humidity on aerosol size. The mass ratio measurements for increasing and decreasing relative humidity over the range $0<f<80$ are presented in Table 6. Also presented are the dry particle density and the threshold water activity.

The effects of relative humidity on dry continental particles are very small for relative humidities less than 70% (Hanel, 1976). A continental particle size distribution at relative humidities 0, 60, 70 and 80% is shown in Fig. 8 depicting very little variation in the distribution due to relative humidity. For decreasing relative humidity (from near 100%), a small hysteresis effect is evident in Fig. 9, where a size distribution for relative humidities 80, 70, 60, and 0% is presented. The shift towards a "dry" particle size distribution occurs at lower relative humidities than that for the maritime aerosol. According to the results of Fitzgerald et al. (1982), sulfate particles

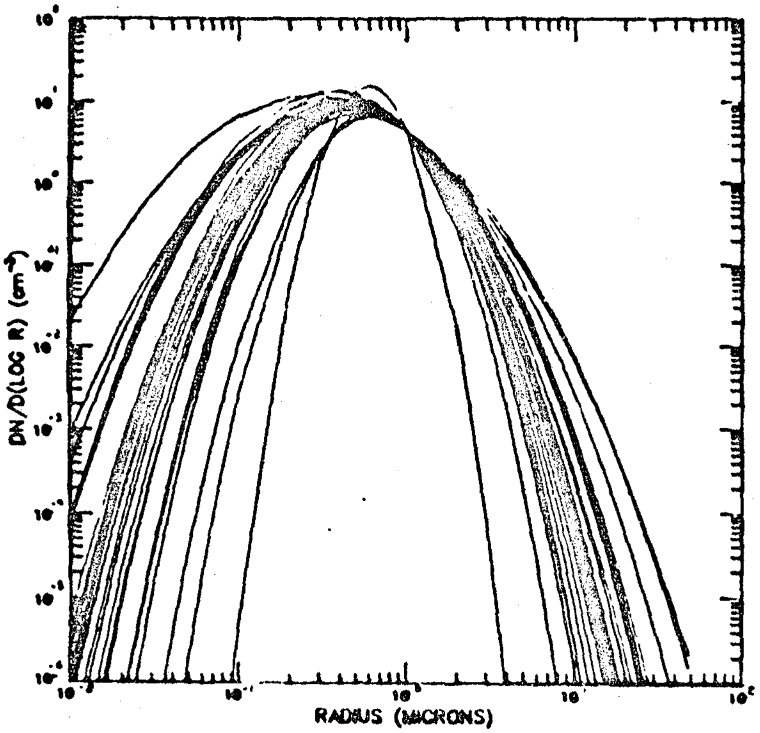

Fig. 7. Twenty-five log normal particle size distributions for the continental (rural) aerosol model. All size distributions are normalized to 4.9 $cm^{-3} \mu m^{-1}$ for $r=0.1 \mu m$ to show relative variability of the particle size distributions.

Table 6. Mass ratio measurements for sulfate and water for increasing and decreasing relative humdiity. The dry particle density and threshold water activity A_{wt} is also included (Hanel and Lehmann, 1980).

MASS RATIO $(NH_4)_2SO_4$

rh	Increasing	Decreasing
20	0.0154	0.0636
30	0.0270	0.0713
40	0.0462	0.2080
50	0.0732	0.3970
60	0.1180	0.6090
65	0.1640	0.9330
70	0.2720	1.0600
75	0.6090	1.2000
80	1.0160	1.4200
A_{wt}	0.7470	0.5760

ρ (gm/cm^{-3}) 1.87

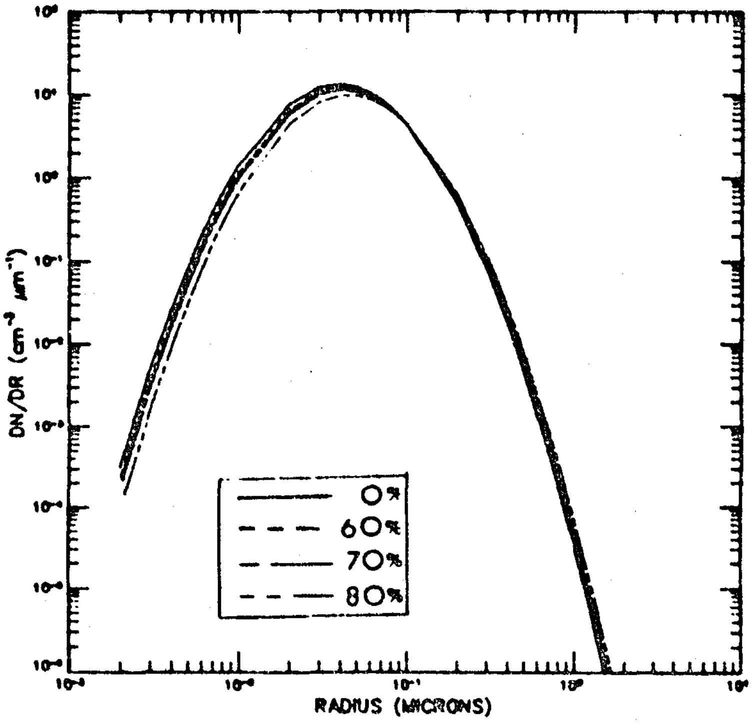

Fig. 8. Continental modeled log normal particle size distribution for the increasing relative humidities 0, 60, 70, and 80%. The curves are normalized to 4 $cm^{-3} \mu m^{-1}$ for $r=0.1 \mu m$.

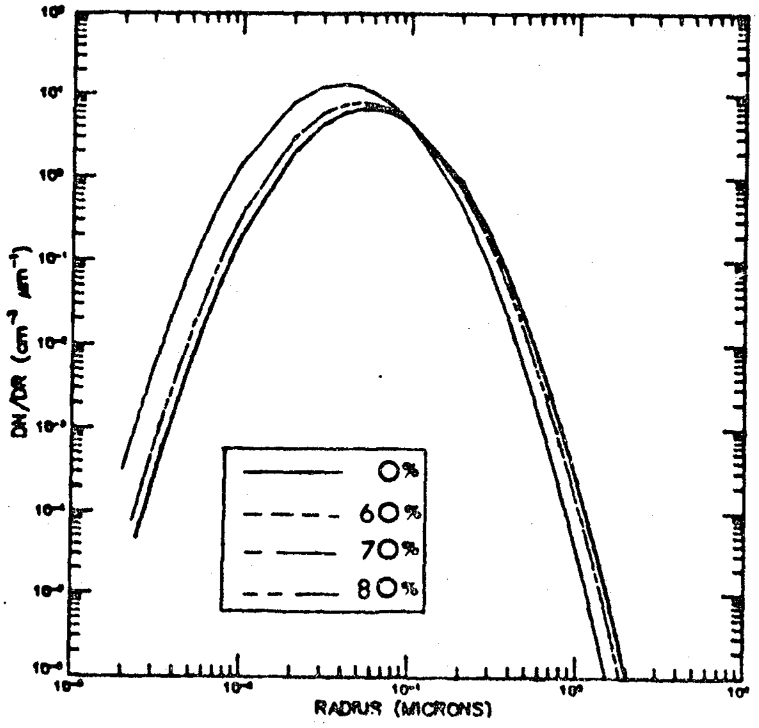

Fig. 9. Continental modeled log normal particle size distribution for the decreasing relative humidities 80, 70, 60, and 0%. The curves are normalized to 4 cm^{-3} μm^{-1} for r=0.1μm.

never return to their original dry size.

III. AEROSOL OPTICAL PROPERTIES

An examination of the optical properties of aerosols with sizes comparable with the wavelength of the incident light is presented. The optical calculations are based on the Mie Theory solution for a homogeneous sphere intercepting a plane light wave. Descriptions of the theoretical Mie formulas for particle scattering are well documented in the literature (Van de Hulst, 1957; Deirmendjian, 1969; Kerker, 1969), and will not be discussed in this paper.

Mie scattering calculations are often very expensive and require a large amount of computing time; therefore a cheaper and faster method of calculating aerosol optical properties has been explored. A Mie theory algorithm developed by Wiscombe (1979) has been tested and used to investigate the backscatter phase function (i.e., phase function at 180°), and the extinction efficiency in the small size parameter range. Average values of the optical properties were calculated over a broad range of refractive indices and found to be relatively smooth functions of size parameter and refractive index. A spline interpolation of these Mie computations at key refractive indices is used to compute backscatter efficiencies and backscatter coefficients rapidly.

3.1 MIE MODEL COMPARISON TEST

The Mie model was tested to determine whether the optical properties were computed accurately. The first test examined the ability of the Mie model to calculate the extinction coefficient and backscatter phase function for the Deirmendjian haze model M. Identical results were calculated by the Mie model within four significant digits for the wavelength 0.45μm.

A comparison between the backscatter calculations derived from the figures of Mugnai and Wiscombe (1980) and the Mie code was used as a second test. Backscatter efficiencies at a few randomly picked size parameters for the wavelength 0.55μm and m=1.5 are shown in Table 7.

Table 7. Comparison between the backscatter efficiency results of Mugnai and Wiscombe (1980) and Mie code based on the Wiscombe algorithm.

SIZE PARAMETER	MIE CODE	RESULTS OF MUGUAI AND WISCOMBE
2.28	0.52	0.52
5.70	2.10	2.10
9.10	4.47	4.50

Based on the above tests, the Mie code has been found to sufficiently calculate aerosol optical properties.

3.2 BACKSCATTER PHASE FUNCTION FOR m=1.33±0i

The backscatter phase function of a homogeneous sphere with a refractive index m=1.33±0i was examined. Periodic fluctuations at small size parameter intervals have been discussed by several authors for the phase function of spherical water drops (Bryant and Cox, 1966; Nussenzveig, 1968; Shipley and Weinman,1978). For a polydispersed aerosol, an average of the backscatter phase function over these periods can be calculated to give the larger scale structure of the phase function. Calculations of the average backscatter phase function at various size parameter increments is presented.

The backscatter phase function has been documented as exhibiting a quasi-periodic structure with a period of $\Delta X_b = 0.83$ at size parameters near 500 (Bryant and Cox, 1966; Shipley and Weinman,1978). Fig. 10, taken from Shipley (1978), demonstrates the periodic structure of the normalized backscatter phase function for the 500 size parameter case. For the case of a water drop, Nussenzveig approximated the period $\Delta X_b = 0.83$ of the backscatter phase function by using the equation:

$$\Delta x_b = \pi / \left(4 \left(m^2 - 1 \right)^{0.5} + \zeta_2 \right) = 0.83 \qquad (5)$$

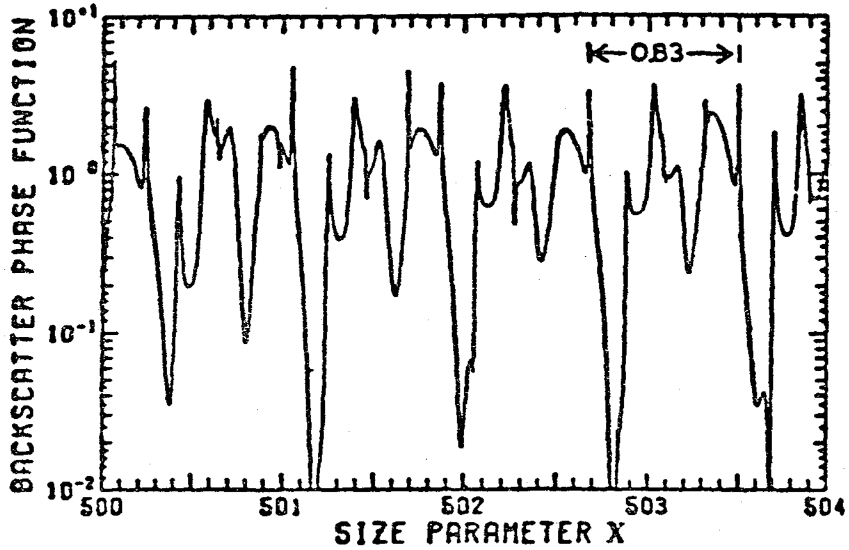

Fig. 10. The normalized backscatter phase function for m = 1.333 and size parameters near 500, showing the quasi-periodic structure with period ΔX_b = 0.83. This data is an extension of the results of Bryant and Cox (1966).

where the parameter $\xi_2 = 0.262$ for $m=1.33\pm0i$. The parameter ξ_2 has only a small dependence on the size parameter.

The backscatter phase function was calculated for the size parameter range $0<X<100$. A resolution of $\Delta X=10^{-2}$ was used for the computations. This resolution is adequate to resolve the details of the backscatter phase function, according to the results of Bryant and Cox (1966). A running mean of the backscatter phase function was performed over an averaging interval of $\Delta X_b = 0.83$. Two larger quasi-periodic oscillations, $\Delta X_c = 1.1$ and $\Delta X_d = 14$, were found in the backscatter phase function as shown in Fig. 11. Similar oscillations were reported by Shipley and Weinman (1978) for $X = 500$.

Since the Mie calculations are so expensive, various size parameter increments were tested to optimize the size parameter calculations for low cost and accuracy. Figs. 12a-d represent the change in the average backscatter phase function for different size parameter increments. The most efficient increment which preserves the feature of the averaged backscatter phase function is shown to be $\Delta X = 0.03$. For example, the peaks of the backscatter phase function features at the size parameters $x=40$, and $x=63.5$ can be seen to decrease for $\Delta X = 0.03$.

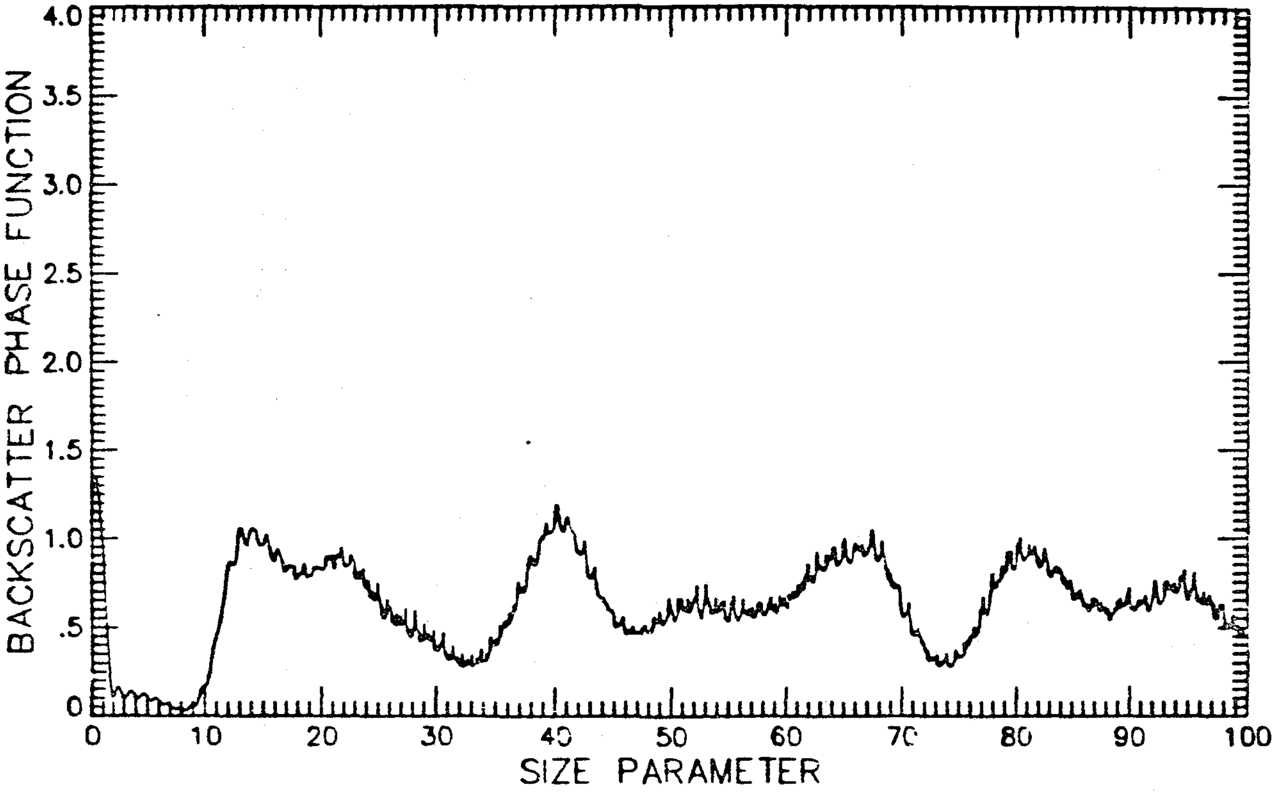

Fig. 11. Running mean of the backscatter phase function for $\Delta X = 0.01$. The running mean was taken over the averaging interval $\Delta X_b = 0.83$.

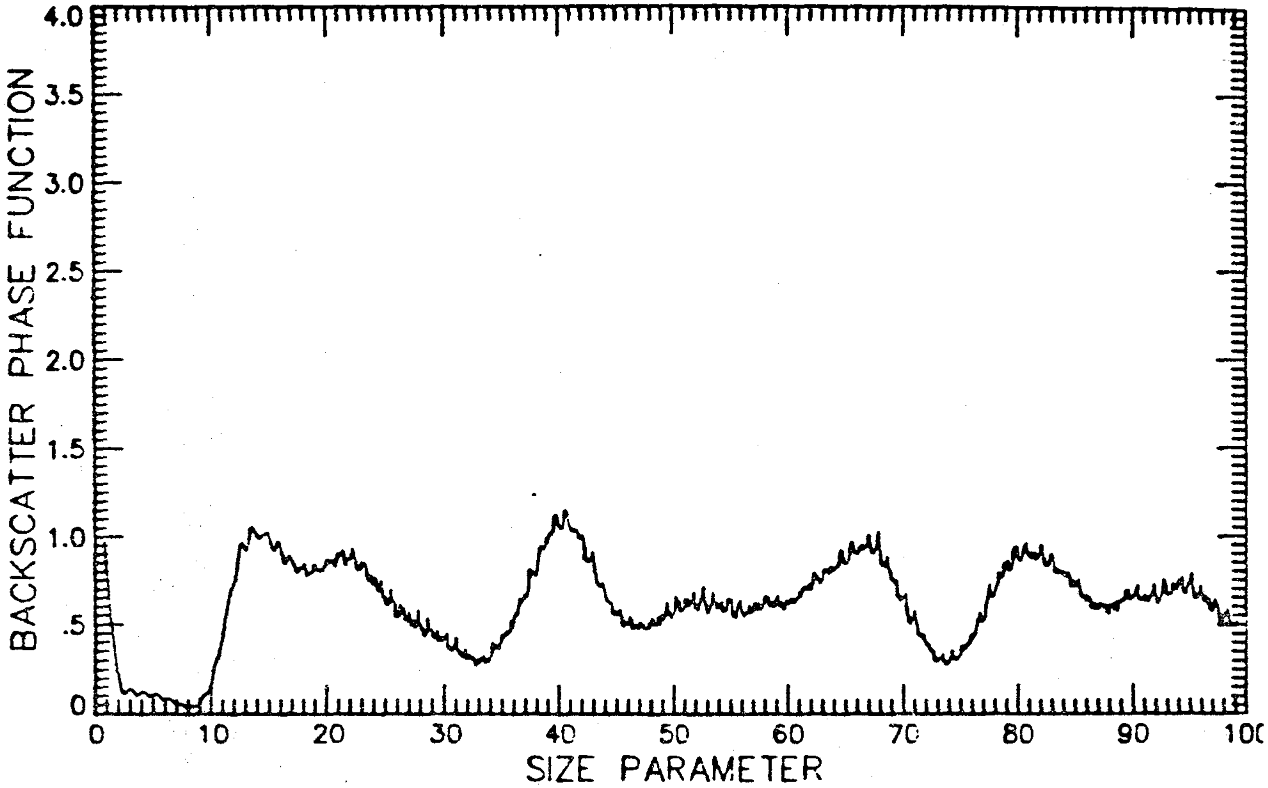

Fig. 12a. Running mean of the backscatter phase function for $\Delta X = 0.02$. The running mean was taken over the averaging interval $\Delta X_b = 0.83$.

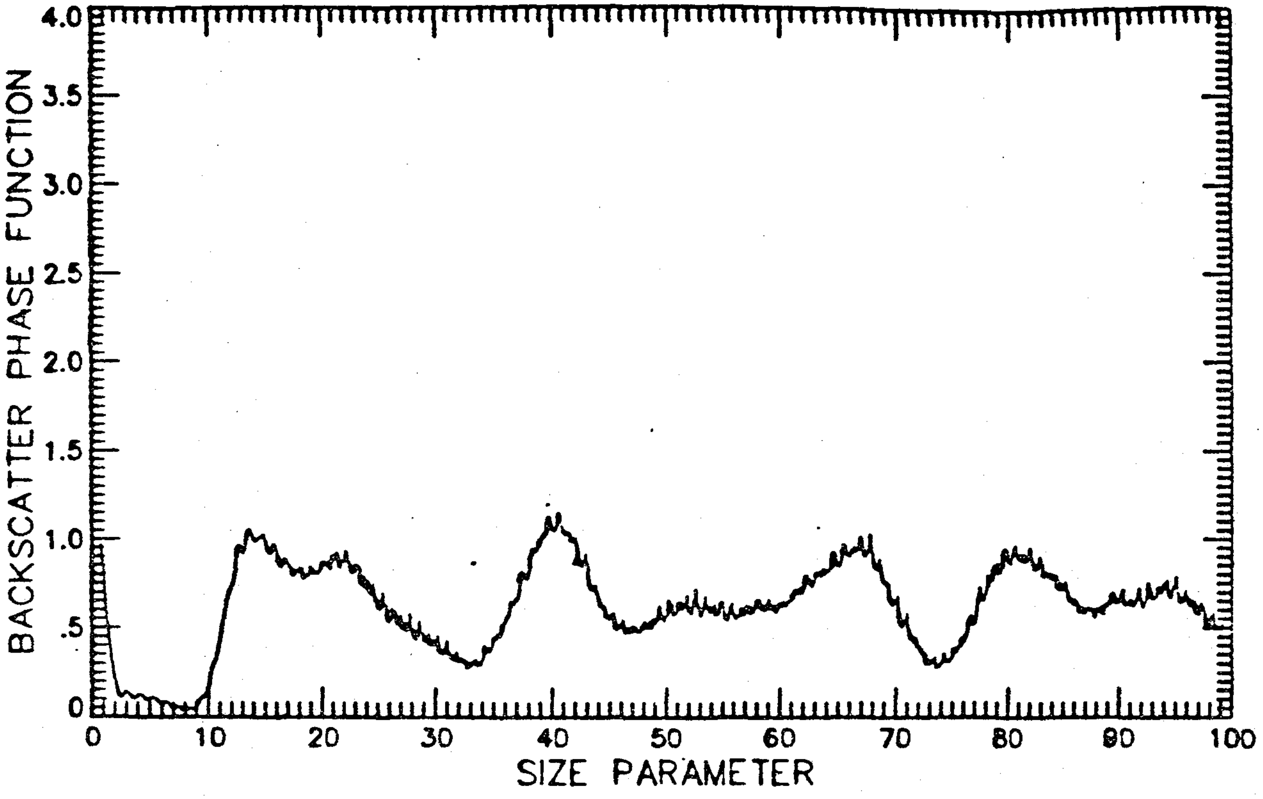

Fig. 12b. Running mean of the backscatter phase function for $\Delta X = 0.03$. The running mean was taken over the averaging interval $\Delta X_b = 0.83$.

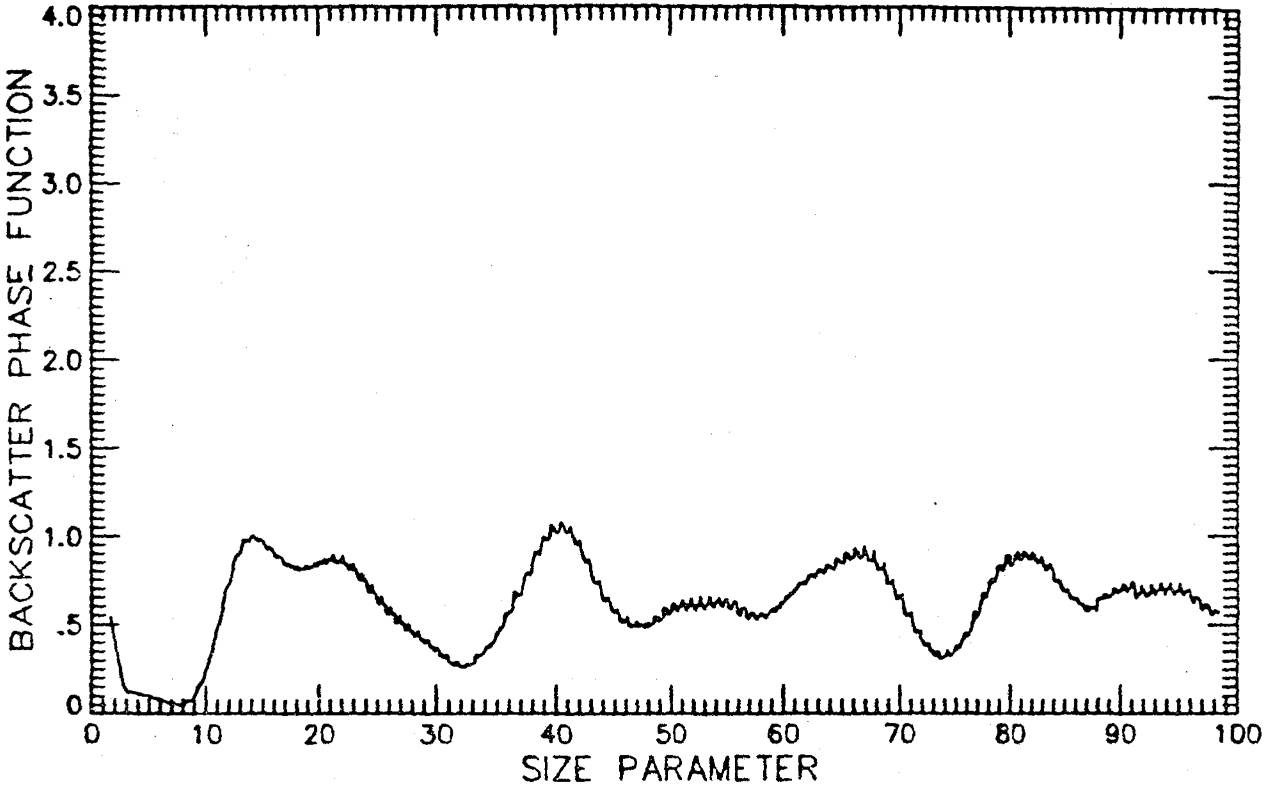

Fig. 12c. Running mean of the backscatter phase function for $\Delta X = 0.04$. The running mean was taken over the averaging interval $\Delta X_b = 0.83$.

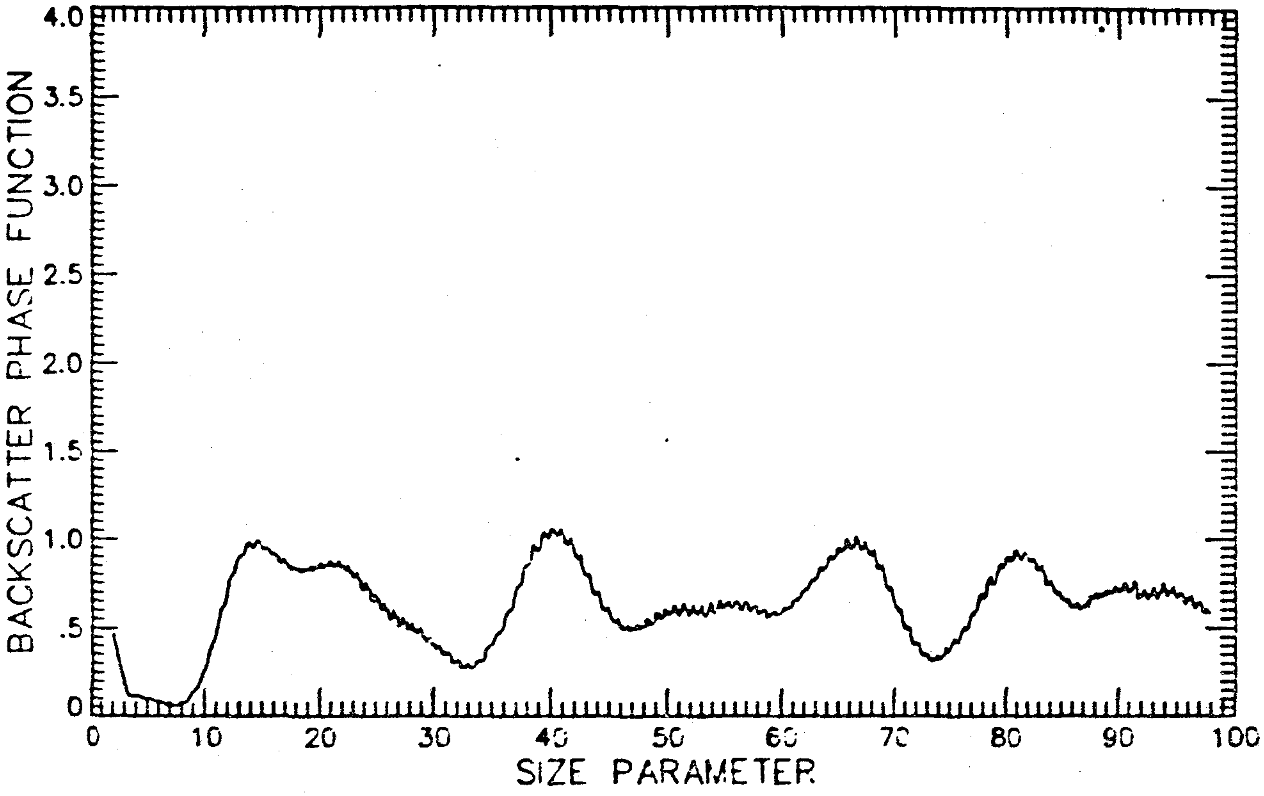

Fig. 12d. Running mean of the backscatter phase function for $\Delta X = 0.05$. The running mean was taken over the averaging interval $\Delta X_b = 0.83$.

3.3 BACKSCATTER COEFFICIENTS FROM SPLINE INTERPOLATIONS

Mie calculations of the averaged backscatter phase functions and extinction efficiencies have been used to compute backscatter coefficients. The Mie calculations were made for small size parameters $0<X<100$ at expected values of refractive indices for continental (sulfate) and maritime (sea-salt) aerosol types. The average optical properties were established to be a relatively smooth function of the expected refractive indices, allowing a spline interpolation to be used to compute backscatter efficiencies. Integration of the backscatter efficiencies over the particle size distributions for each wavelength were made, and thus values for the backscatter coefficients were determined as a function of wavelength.

The backscatter phase functions and extinction efficiencies were averaged using the appropriate averaging interval (ΔX_b) for each expected refractive index. The values of ΔX_b were derived from Nussenzvieg's equation (Equation 5) and are presented in Table 8.

The averages of the backscatter phase function and extinction efficiencies were computed at 2.5 size parameter increments for $\Delta X = 0.03$. The 2.5 size parameter increment was used as the midpoint of the averaging interval as shown in the example on the following page.

Table 8. Period ΔX_b of the backscatter phase function oscillations for various refractive indices.

m	ΔX_b
1.33	0.83
1.35	0.81
1.37	0.78
1.39	0.76
1.41	0.74
1.43	0.72
1.45	0.70
1.47	0.69
1.49	0.67
1.51	0.66
1.53	0.64
1.55	0.63
1.57	0.62
1.59	0.60

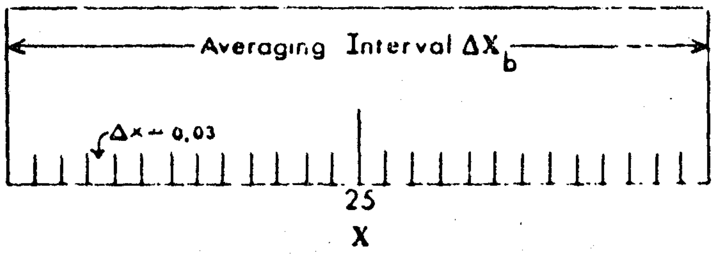

A contour analysis of the averaged backscatter phase function for the expected range of refractive indices is shown in Fig. 13. The average backscatter phase function appears to be a relatively smooth function of the refractive index at these small size parameters. A similar smooth function was apparent for the average extinction efficiencies, thus, allowing average values of the backscatter phase functions and extinction efficiencies to be computed by a spline interpolation.

For a given wavelength and refractive index, a spline interpolation of the averaged backscatter phase function and extinction efficiency values allows for the computation of backscatter efficiencies at small size parameters. Backscatter efficiencies were derived by the expression:

$$Q_{\pi} = \mathbb{P}_{\pi} Q_e \qquad (6)$$

where

Q_{π} is the backscatter efficiency,

Q_e is the averaged extinction efficiency,

$\mathbb{P}_{\pi}$ is the averaged backscatter phase function.

The backscatter coefficients were derived by integrating the backscatter efficiencies over the log normal particle size distributions as shown on page 48.

ORIGINAL PAGE IS
OF POOR QUALITY

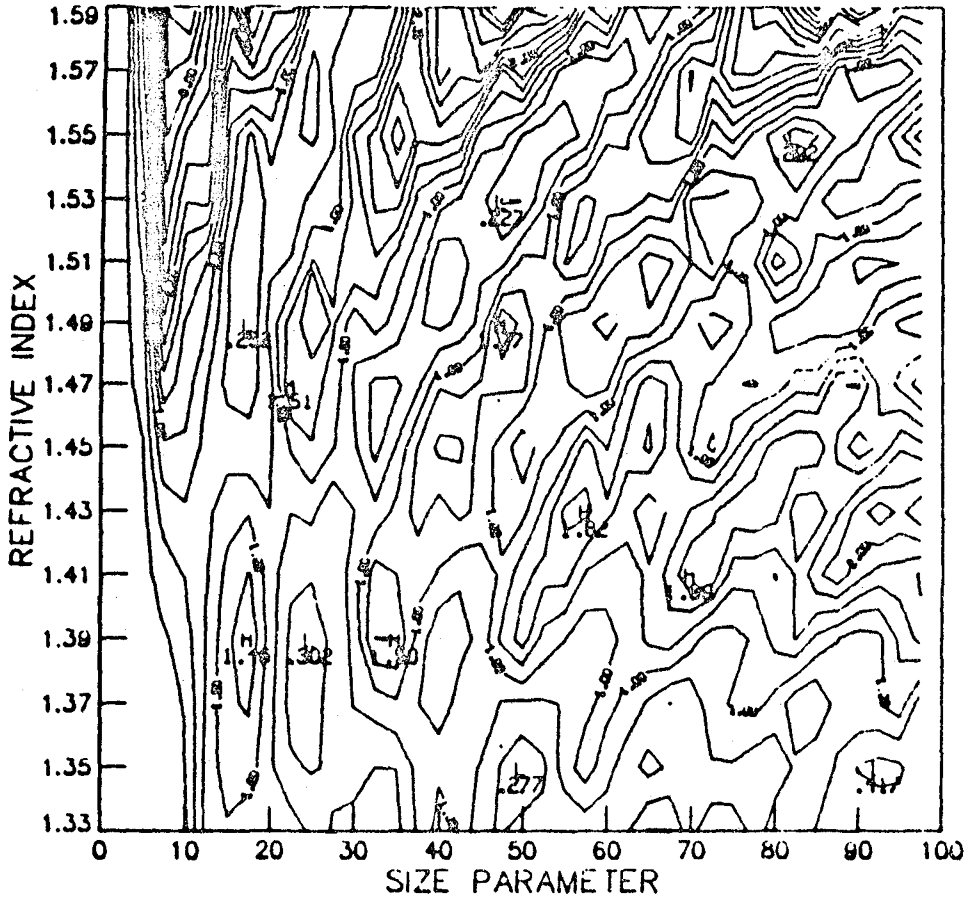

Fig. 13. Contour analysis of the averaged backscatter phase function at small size parameters. The running mean for each phase function was taken over the averaging interval Δx_b = 0.83, 0.81, 0.78, 0.76, 0.74, 0.72, 0.70, 0.69, 0.67, 0.66, 0.63, 0.62, 0.61, 0.60 for refractive indices of 1.33, 1.35, 1.37, 1.39, 1.41, 1.43, 1.45, 1.47, 1.49, 1.51, 1.53, 1.55, 1.59, respectively.

$$\beta_\pi(\lambda) = \int_{r_1}^{r_2} \pi r \; Q_\pi(m,r) \frac{dN}{dr} dr \qquad (7)$$

where

β_π is the volume backscatter coefficient,
r is the radius,
$\frac{dN}{dr}$ is the particle size distribution.

The backscatter efficiencies derived from the interpolated backscatter phase functions and extinction efficiencies, were used to compute backscatter coefficients as a function of wavelength. The range of wavelengths used on the calculations was $0.2<\lambda<2.0$ μm.

IV. RESULTS AND DISCUSSION

Backscatter calculations for two key aerosol classes were performed as a function of wavelength. These calculations included variations due to the natural variability of particle size distribution, refractive index, and relative humidity. The backscatter coefficients were calculated for refractive indices characteristics of sea-salt and sulfate aerosol compositions, each over twenty-five particle size distributions and seventeen relative humidities varying from 0 to 80%.

Optical properties of atmospheric aerosols are weighted by the aerosol size distribution, and aerosol scattering is very sensitive to particle radius size variability (Deirmendjian, 1969). Aerosol size distributions vary in the atmosphere due to variations in meteorological conditions, sources, sinks, geographical locations, and time of year. For very small aerosol radii (i.e., Rayleigh scatterer with $r<<1$), the scattering pattern is symmetric. As particle radii increase, the scattering pattern becomes asymmetric with more scattering in the forward direction. Once the particle radii exceed the incident light wavelength, troughs and ridges begin to appear in the scattering pattern and most of the energy is scattered into the forward and backward directions (Paltridge et al., 1976). Thus, aerosol volume backscatter is very sensitive to size, and it is therefore sensitive to natural variability of the particle size distribution. Figures 14a and 14b demonstrate this natural variability, showing backscatter coefficients for 25 simulated dry particle size distributions based on available measurements from Chapter II. The backscatter curves were normalized at a wavelength 0.9μm to highlight the relative wavelength dependence.

The volume backscatter coefficient β_π is assumed to follow a power law dependence with wavelength, such that

$$\beta_{\pi_\lambda} = \beta_{\pi_{\lambda_0}} \left(\frac{\lambda}{\lambda_0}\right)^{-\delta} \tag{8}$$

This assumption allows a direct calculation of the exponent given the backscatter coefficient at two sufficiently separated wavelengths. Backscatter coefficients for both sea-salt and sulfate aerosol compositions were calculated at the wavelengths 0.3, 0.4, 0.55, 0.7, 0.9, 1.05, 1.35, 1.5, and 1.8μm. The power law wavelength dependences were computed by linear regression to the logarithm of these backscatter calculations over four different wavelength intervals. The wavelength intervals are 0.3-0.5 μm, 0.55-0.9μm, 0.9-1.35μm, and 1.35-1.8μm, and they will be referred to as wavelength regions 1, 2, 3, and 4, respectively.

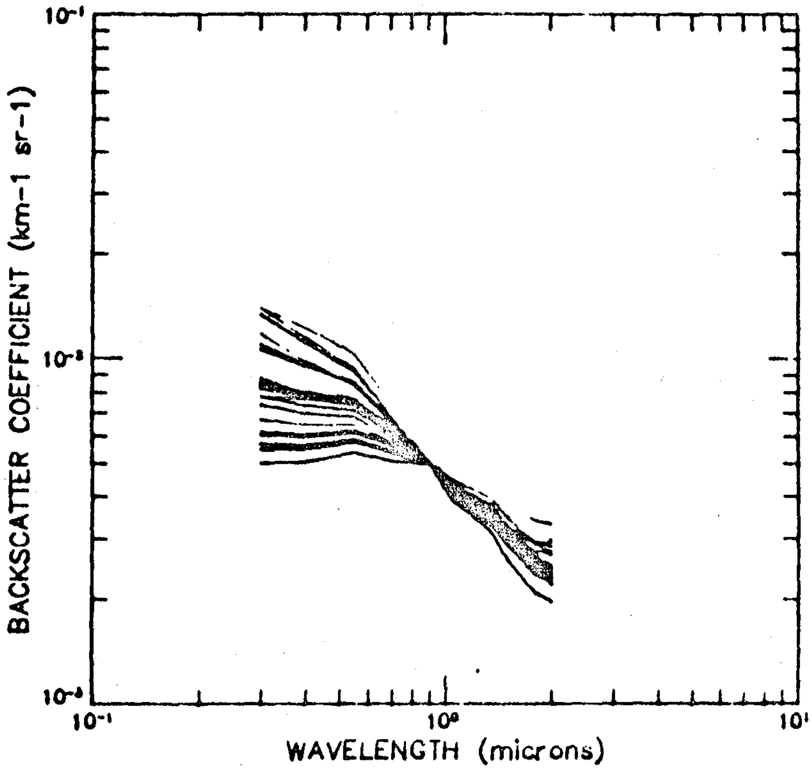

Fig. 14a. Maritime (sea-salt) backscatter coefficients as a function of wavelength for twenty-five dry log normal particle size distributions. The backscatter coefficients were normalized to 3.7 E-4 ($km^{-1}sr^{-1}$) at $r=0.9\mu m$ to highlight the relative wavelength dependence.

ORIGINAL PAGE IS
OF POOR QUALITY

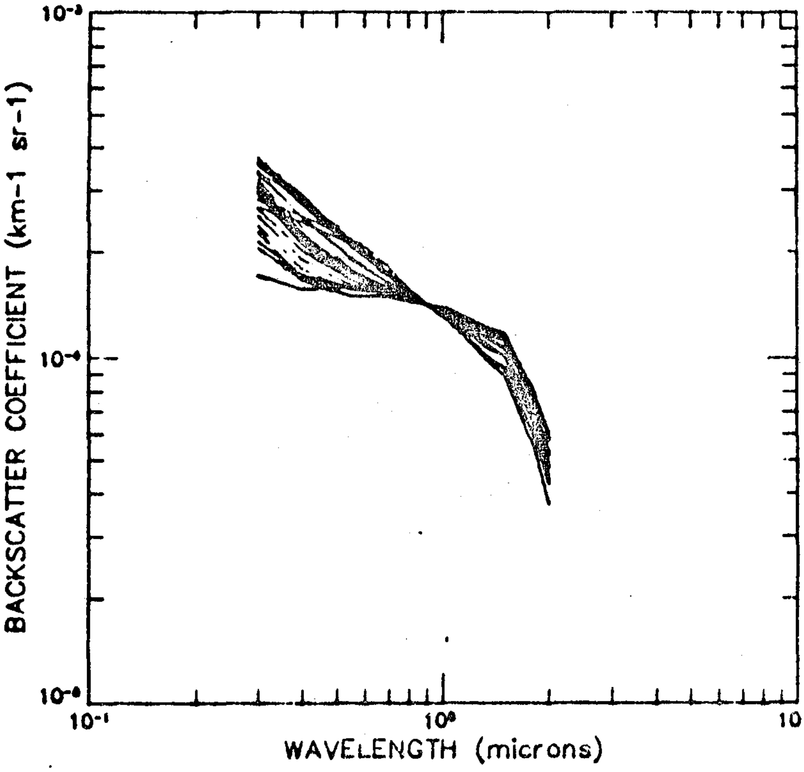

Fig. 14b. Continental (sulfate) backscatter coefficients as a function of wavelength for twenty-five dry log normal particle size distributions. The backscatter coefficients were normalized to 1.6 E-4 ($km^{-1}sr^{-1}$) at $r=0.9\mu m$ to highlight the relative wavelength dependence.

The theoretical backscatter wavelength dependences for sea-salt and sulfate aerosol compositions can now be used to distinguish the two compositions. The mean and one standard deviation of the δ variations was computed in each of the four wavelength regions. If the mean δ values are separated by more than the sum of their standard deviations, then the two aerosol classes are assumed to be distinguishable. Backscatter discrimination between sea-salt and sulfate aerosols with the same relative humidity history is examined in section 4.1. Backscatter discrimination for sea-salt and sulfate aerosols with different relative humidity histories is examined in section 4.2.

4.1 COMPARISON OF SEA-SALT AND SULFATE AEROSOLS AT IDENTICAL RELATIVE HUMIDITIES

The backscatter wavelength dependence of sea-salt and sulfate aerosol particles at the same relative humidity has been compared to determine which wavelength regions are best suited to distinguish between the two aerosol compositions. The comparison was made for increasing relative humidities from 0 to 80%, with initially dry conditions, and for decreasing relative humidities from 80 to 30%, with initially saturated conditions. As relative humidity increases, the optical properties of both aerosol compositions approaches the characteristics of water and the use of δ for aerosol discrimination becomes less attractive. It is also noteworthy that the wavelength regions where sea-salt and sulfate aerosol compositions can be discriminated by backscatter is different for increasing and decreasing relative humidities due to the hysteresis effect of deliquescent materials.

For the relative humidity increasing from initially dry conditions, the water uptake by sulfates and sea-salt particles below 50% relative humidities is very small, and the wavelength dependence of backscatter does not vary with relative humidity. Figures 15-18 show the range of δ variations for sea-salt and sulfate aerosol compositions undergoing increasing and decreasing relative humidity variations in the four wavelength regions. Each block depicts the δ mean (at the center of the block) and one standard deviation about the mean. By the definition of distinguishability presented earlier, these figures demonstrate that the two aerosol compositions (under dry conditions) can be discriminated by δ in the wavelength regions 1 and 4. The variability of δ at zero relative humidity is due solely to variation in the particle size distributions. As relative humidity increases to 50% for both aerosol compositions, only a small shift in δ is apparent. For 50% relative humidity, Figures 15 and 18 show that the δ discrimination is still possible in wavelength regions 1 and 4. However, it should be noted that the δ discrimina-

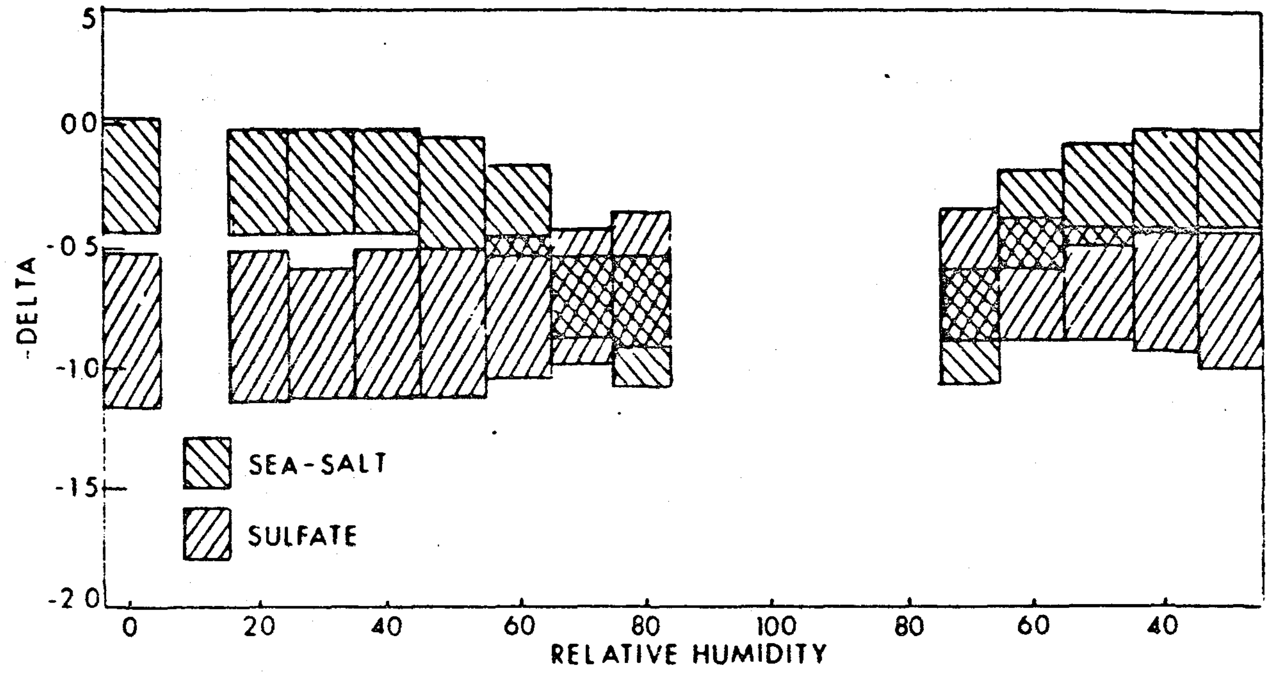

Fig. 15. Comparison of the backscatter wavelength dependence (δ) in wavelength region 1 for sea-salt and sulfate particles undergoing relative humidity variations. Each block represents the mean value (at the center of the block) ± one standard deviation.

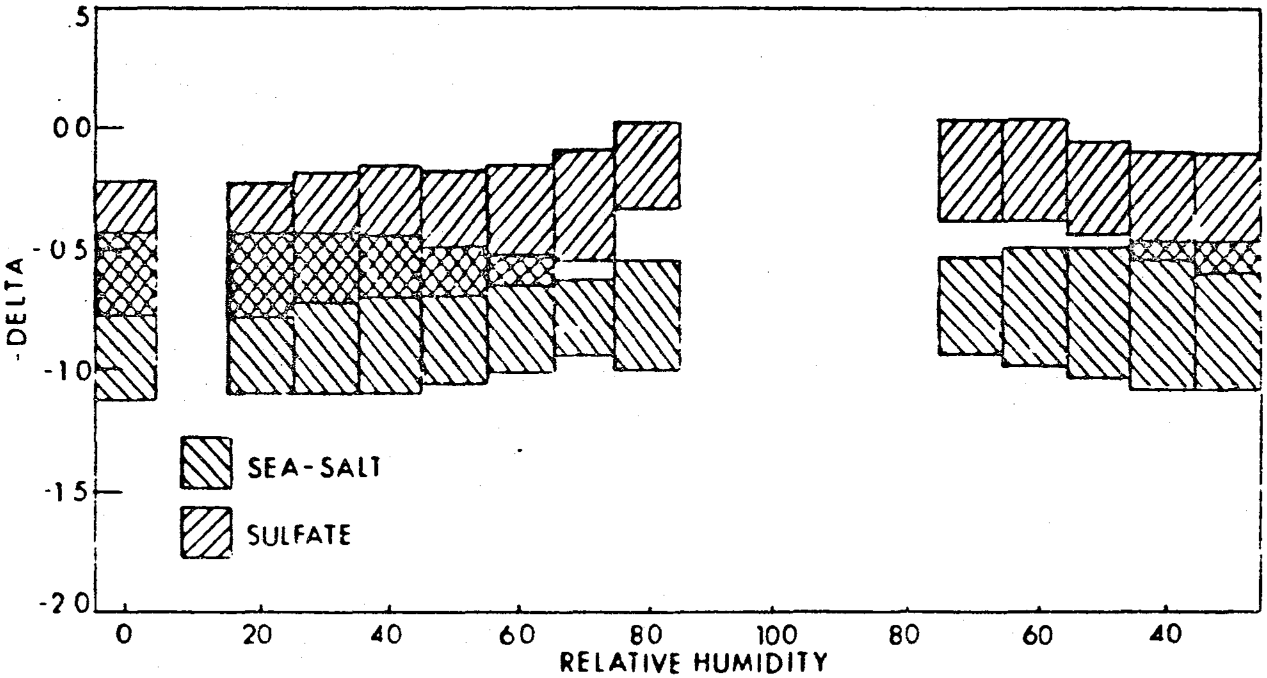

Fig. 16. Comparison of the backscatter wavelength dependence (δ) in wavelength region 2 for sea-salt and sulfate particles undergoing relative humidity variations. See Fig. 15.

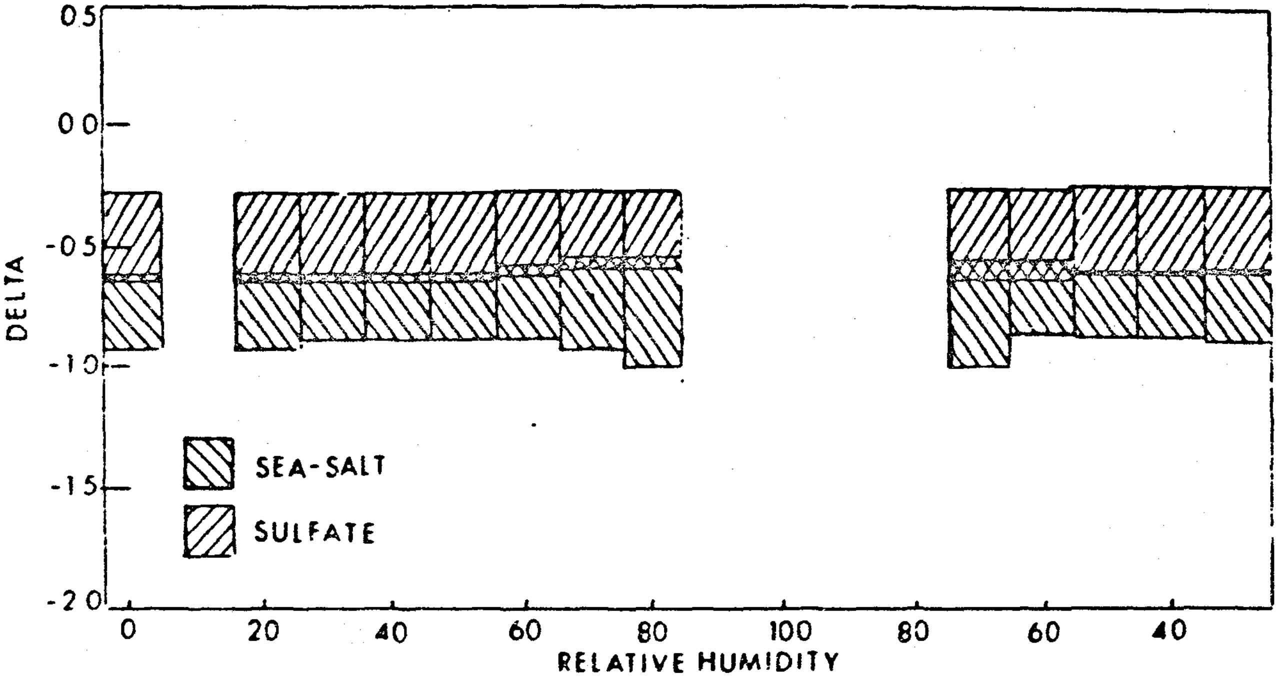

Fig. 17. Comparison of the backscatter wavelength dependence (δ) in wavelength region 3 for sea-salt and sulfate particles undergoing relative humidity variations. See Fig. 15.

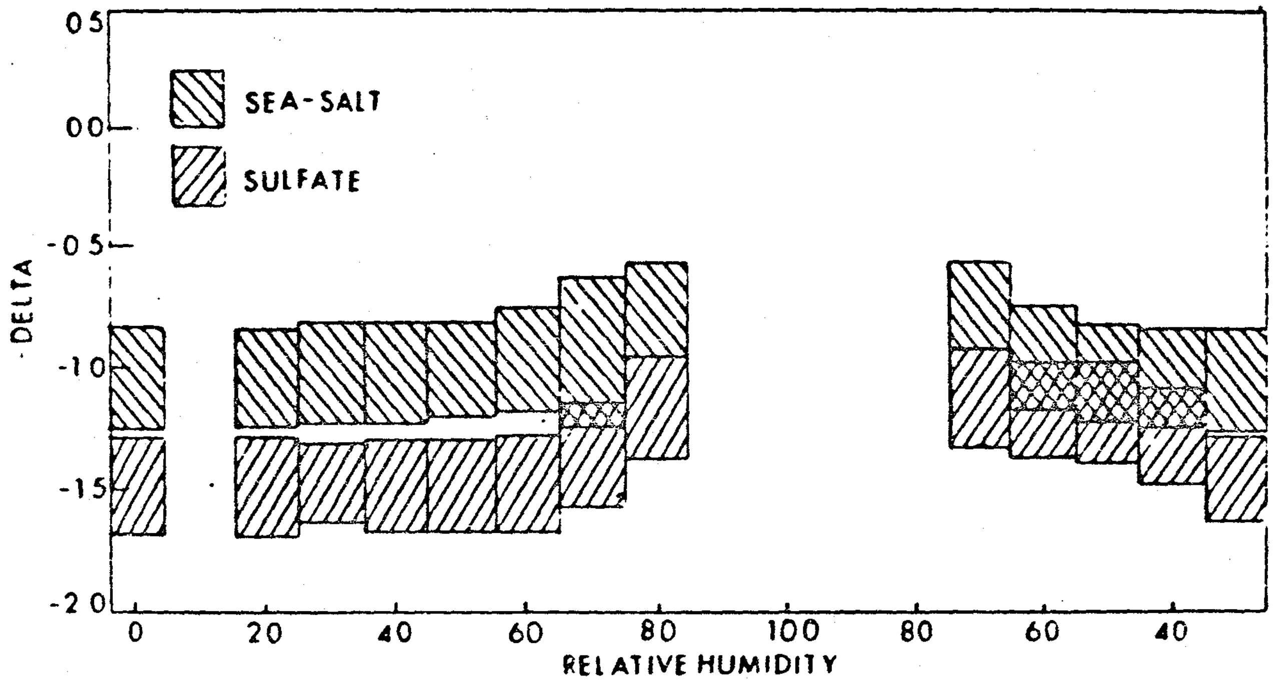

Fig. 18. Comparison of the backscatter wavelength dependence (δ) in wavelength region 4 for sea-salt and sulfate particles undergoing relative humidity variations. See Fig. 15.

tion in wavelength region 1 is approaching the limits of the distinguishability criterion.

The critical deliquescent point of the aerosol particles is approached as the relative humidity approaches 60%. The critical relative humidity of a deliquescent material is that relative humidity where a dry salt changes into a salt solution. The distribution of δ for both aerosol composition starts to shift in all four wavelength regions. The increase in the average sea-salt aerosol particle radius at high relative humidity is much larger than that for sulfate aerosol as demonstrated in Figure 3. Thus, most of the δ shifts occur first for the sea-salt composition. This is demonstrated in Figure 15, where the sea-salt δ in wavelength region 1 begins to become more negative (steeper slope), while the sulfate δ does not change significantly. At 60% relative humidity, sea-salts and sulfate aerosols are distinguishable only in wavelength region 4 as seen in Figure 18.

Once relative humidity increases beyond the critical relative humidity of a deliquescent material (near 70% and above), that material will begin to acquire the physical properties of water, and the ability to distinguish aerosol composition by δ becomes more difficult. Figures 15-18 show that at these higher relative humidities the distributions, except in the sulfate wavelength region 2, are converging towards a common range. As aerosol particles become larger they scatter more uniformly with wavelength (Van de Hulst, 1957). The shift in wavelength region 2 for sulfates is towards a more positive slope than for the δ distribution found for sea-salts. These results indicate that the δ discrimination between sea-salt and sulfate aerosols at higher relative humidities (70%) is possible in wavelength region 2.

As relative humidity decreases from saturated conditions, deliquescent particles will decrease in size at a much slower rate than their original growing rate. This is due to a deliquescent material's nature to supersaturate with respect to the material in solution. A relative humidity decreasing from saturated conditions was used in the calculations to insure a broad hysteresis loop for each composition. Since decreasing relative humidity affects particle radius size and refractive index differently than increasing relative humidity, the backscatter wavelength dependence will not be the same. For sea-salt particles, most of the changes in the distribution of δ occurs at relative humidities between 80% and 60%. Once the particles dry out at relative humidities less than 60%, the δ distribution changes very little and returns to the original dry state distribution. For the sulfate particles, the shift in δ at higher relative humidities (80-50%) is smaller than the shift found for sea-salt. For decreasing relative humidities below 50%, sulfate particles never lose all of the added water. A comparison of the sulfate test cases at 30% relative humidity for increasing and decreasing relative humidity is shown in Figure 19, demonstrating that sulfate particles do not return to their original dry δ distributions. The shifts found in the two aerosol δ distributions are characteristic of their hysteresis curves presented in Figure 3.

For relative humidities decreasing to 50%, the ability to discriminate between the aerosol compositions, sea-salts and sulfates, within one standard deviation of their δ means is possible only in the wavelength region 2. This is quite different from the results for increasing relative humidity, where discrimination in wavelength region 2 was impossible until 70% relative humidity. The wavelength region difference between the increasing and decreasing relative humidity test cases is related to the extra water that both aerosol compositions contain at decreasing relative humidities. As relative humidity decreases to 40%, a shift occurs in the sulfate δ distribution towards a more negative slope in the wavelength region 2. The two aerosol compositions are no longer distinguishable in any of the four wavelength regions. As relative humidity continues to decrease, the sea-salt δ values return to their original dry distributions. Figure 16 shows the sulfate δ distribution shifting toward those of sea-salt in wavelength region 2. The δ distribu-

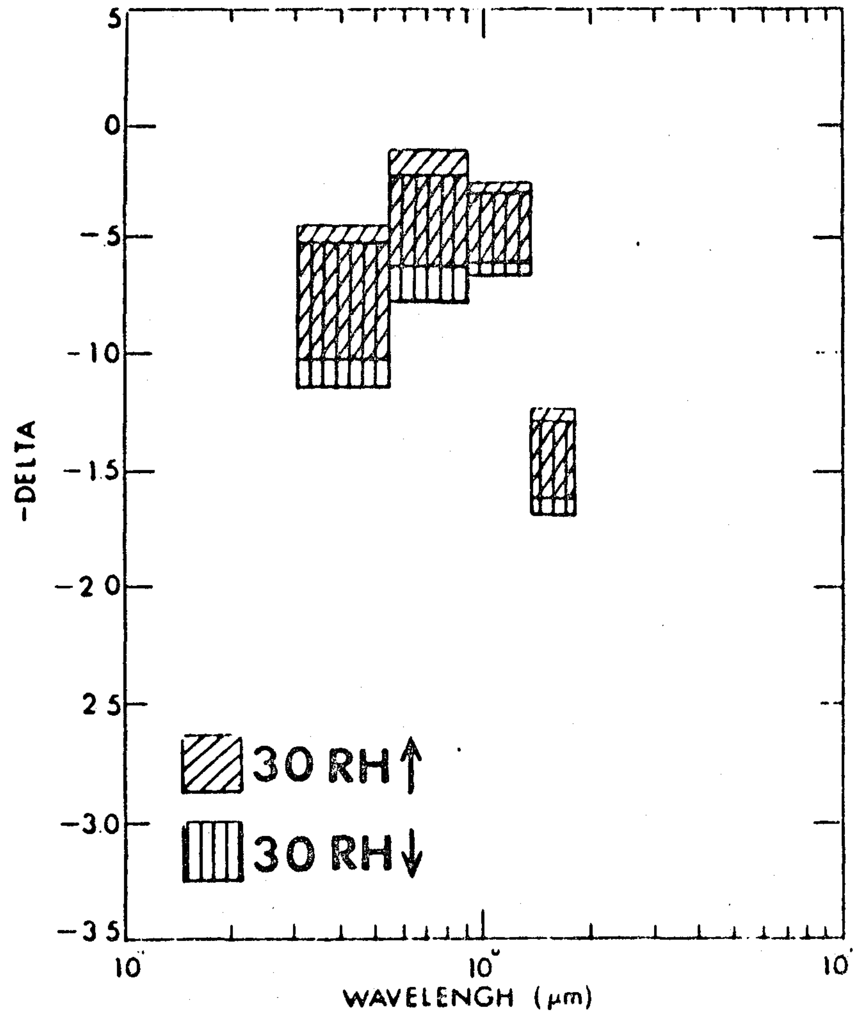

Fig. 19. Comparison of the backscatter wavelength dependence σ of sulfate aerosols at an increasing relative humidity 30% and a decreasing relative humidity 30%. See Fig. 15.

tions for both aerosol compositions shift away from each other in wavelength regions 1 and 4, thus allowing discrimination between sea-salt and sulfate aerosols for decreasing relative humidity at 30%.

4.2 SEA-SALT AND SULFATE AEROSOLS AT DIFFERENT RELATIVE HUMIDITIES

The theoretical backscatter wavelength dependence of sea-salt and sulfate aerosol compositions has been compared at different relative humidities to determine which wavelength regions can best discriminate between the two aerosol compositions. The δ comparisons were made for an aerosol composition at a constant dry relative humidity and the other aerosol composition undergoing increasing and decreasing relative humidity variations. This comparison applies to dry aerosol layers in the free troposphere with most aerosols in the mixed layer. Such aerosol layers were observed in the lower troposphere during the Global Tropospheric experiment (Browell and Shipley, 1982).

A comparison between the wavelength regions that can best discriminate between sulfate aerosols and sea-salt aerosols at increasing and decreasing relative humidity is presented in Figures 20-23. In section 4.1, it was shown that for zero relative humidity, the two compositions were distinguishable by δ in the wavelength regions 1 and 4. As relative humidity was allowed to increase for the sea-salt aerosols (from 0 to 50%), very little water uptake

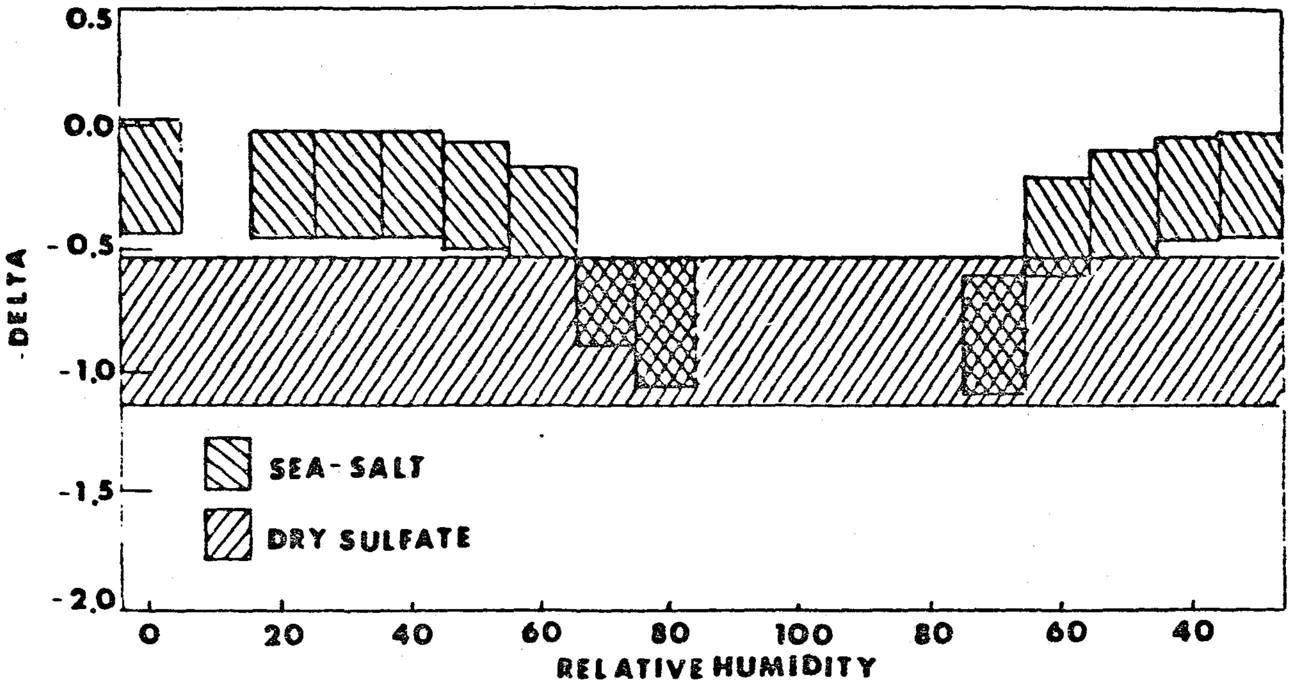

Fig. 20. Comparison of the backscatter wavelength dependence (δ) in wavelength region 1 for dry sulfate and sea-salt particles undergoing relative humidity variations. See Fig. 15.

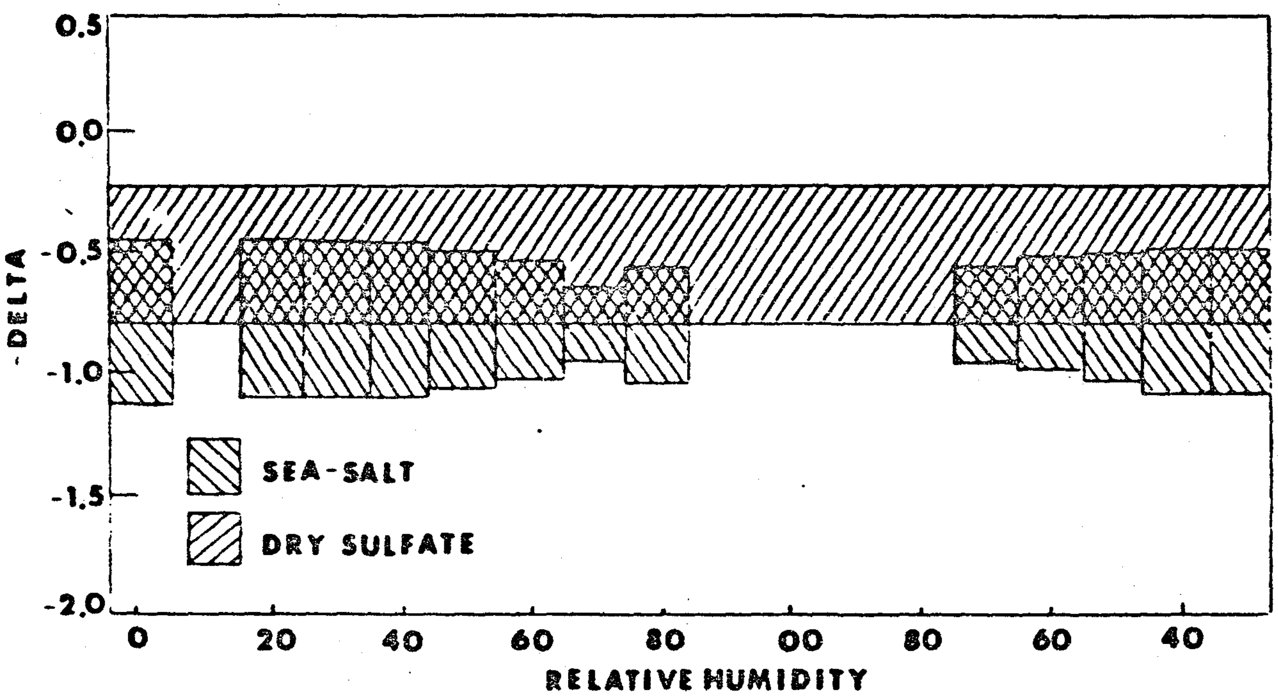

Fig. 21. Comparison of the backscatter wavelength dependence (δ) in wavelength region 2 for dry sulfate and sea-salt particles undergoing relative humidity variations. See Fig. 15.

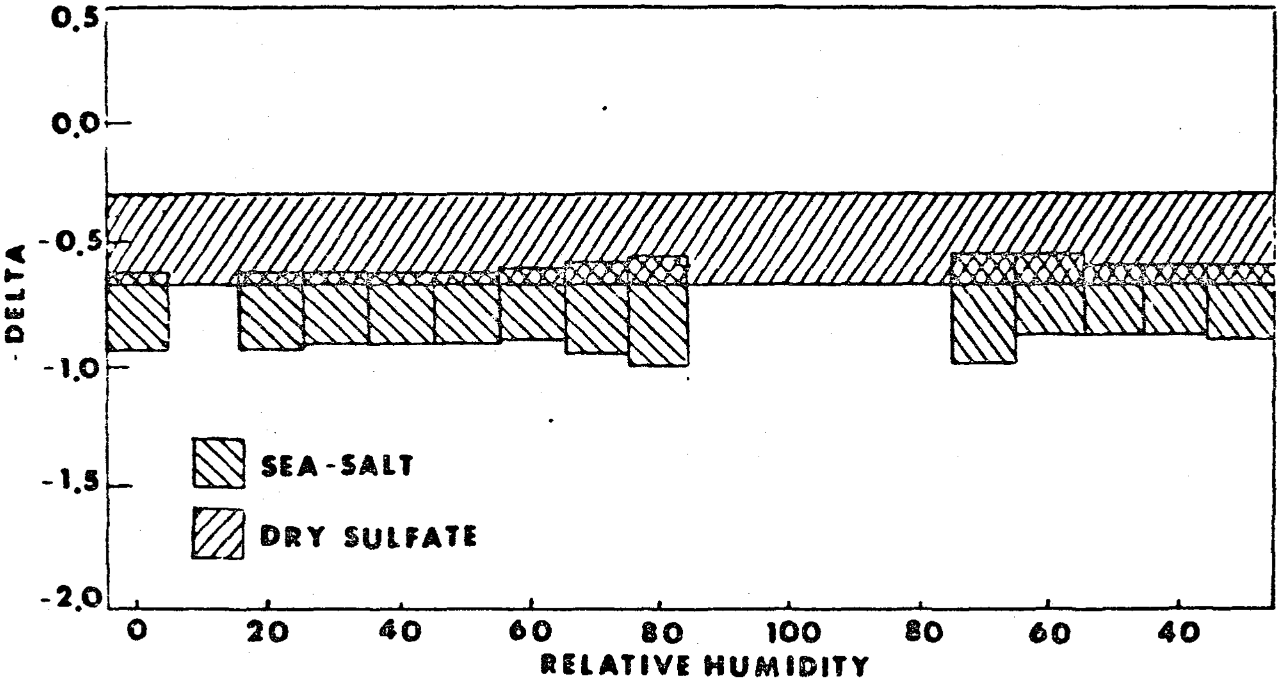

Fig. 22. Comparison of the backscatter wavelength dependence (δ) in wavelength region 3 for dry sulfate and sea-salt particles undergoing relative humidity variations. See Fig. 15.

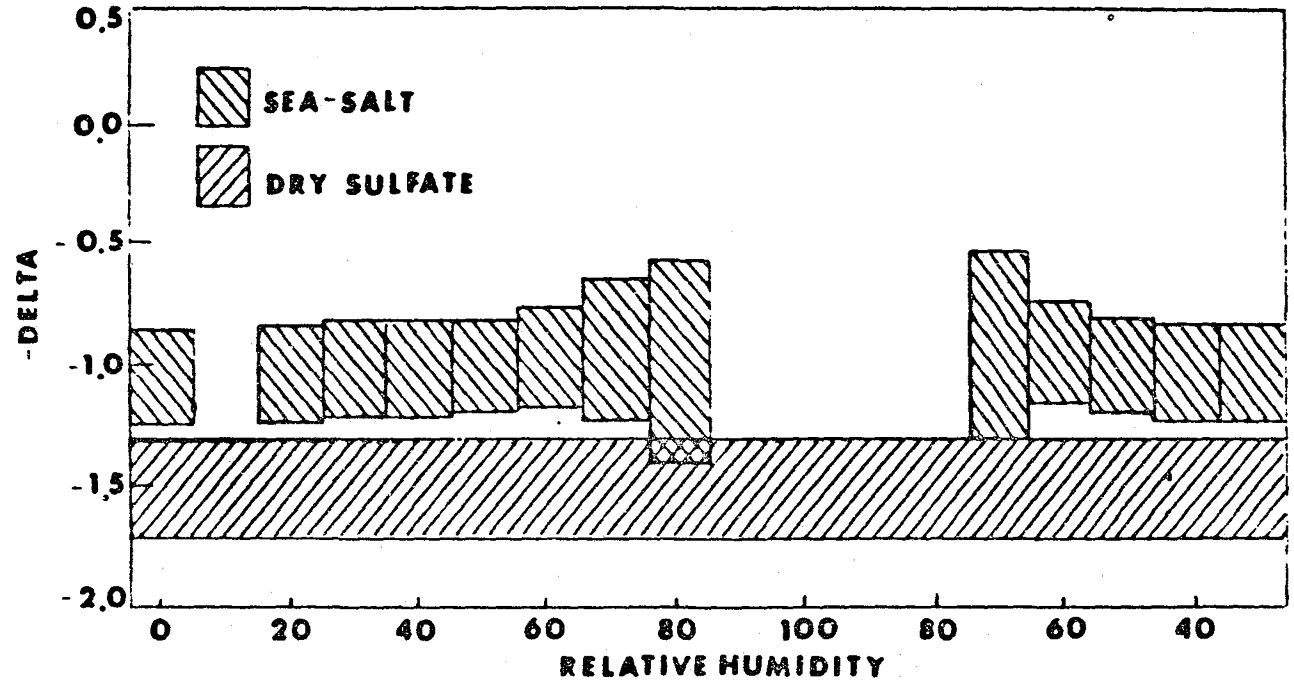

Fig. 23. Comparison of the backscatter wavelength dependence (δ) in wavelength region 4 for dry sulfate and sea-salt particles undergoing relative humidity variations. See Fig. 15.

by the particles was apparent. Figures 20 and 23 demonstrate that for sea-salt particles at 50% relative humidity, the wavelength regions where δ can distinguish the aerosol compositions is identical to the zero relative humidity comparison test case (i.e., wavelength regions 1 and 4).

As relative humidity increases from 50%, the distribution of sea-salt δ converges toward a common range. For the 60% sea-salt test case, shown in Figure 20, values in the wavelength region 1 have shifted towards those of dry sulfate, and thus only wavelength region 4 can be used to discriminate the two compositions. Once the critical relative humidity for sea-salts is reached (70%), the range of δ in wavelengths region 4 increases. Figures 20-23 shows that for relative humidities 75% or above, the two aerosol δ distributions are no longer distinguishable within the one standard deviation criteria for any of the wavelength regions.

For decreasing relative humidity from saturated conditions, the two aerosols compositions cannot be distinguished by δ for any of the four wavelength regions. As relative humidity decreases from 70% to 60%, the spread of δ for the sea-salt aerosol in the wavelength 4 decreases, thus allowing the dry sulfates to be discriminated from the sea-salt particles by δ in the wavelength region 4 as shown in Figure 23. Once the relative humidity decreases below 60%, the sea-salt particles start to dry out and discrimination is possible in the wavelength region 1. As relative humidity continues to decrease to 30%, the δ discrimination can identify the two aerosols compositions in the wavelength regions 1 and 4.

The wavelength regions that best distinguish the dry sulfates from sea-salt particles at low relative humidities are identical for both of the increasing and decreasing relative humidity cases. This is characteristic of the hysteresis curve for the sea-salt aerosol since sea-salts return to their original dry size at low decreasing relative humidities.

The second situation considered was the comparison of dry sea-salt aerosols with sulfate particles undergoing increasing and decreasing relative humidity variations as shown in Figures 24-27. As mentioned in section 4.1, the water uptake by sulfate particles is very small at low relative humidities. Figures 24 and 27 demonstrate that the small water uptake has little effect on the δ discriminations, since the compositions can be distinguished in wavelength regions 1 and 4 at 20% and 50% relative humidities.

As relative humidity increases to 60% and above, the sulfate δ in the wavelength region 3 shifts away from that for dry sea-salts, as seen in Figure 26, allowing the δ discrimination to be possible in the wavelength regions

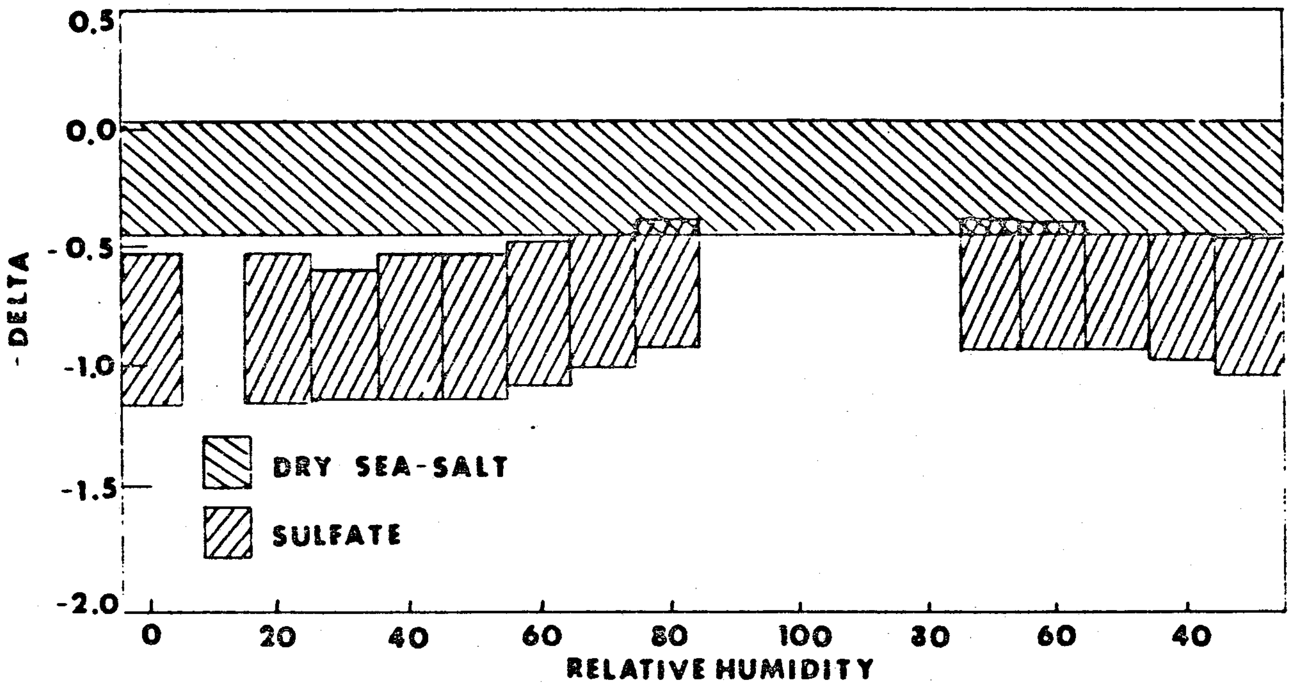

Fig. 24. Comparison of the backscatter wavelength dependence (δ) in wavelength region 1 for dry sea-salt and sulfate particles undergoing relative humidity variations. See Fig. 15.

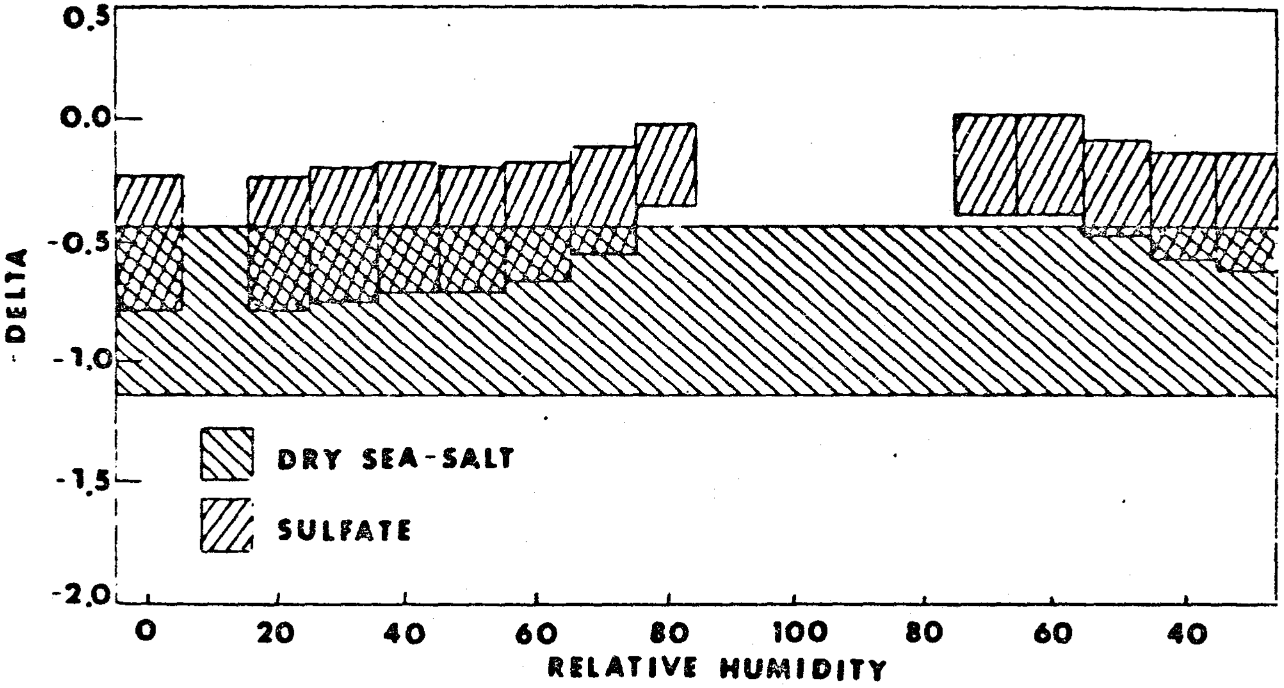

Fig. 25. Comparison of the backscatter wavelength dependence (δ) in wavelength region 2 for dry sea-salt and sulfate particles undergoing relative humidity variations. See Fig. 15.

ORIGINAL PAGE IS OF POOR QUALITY

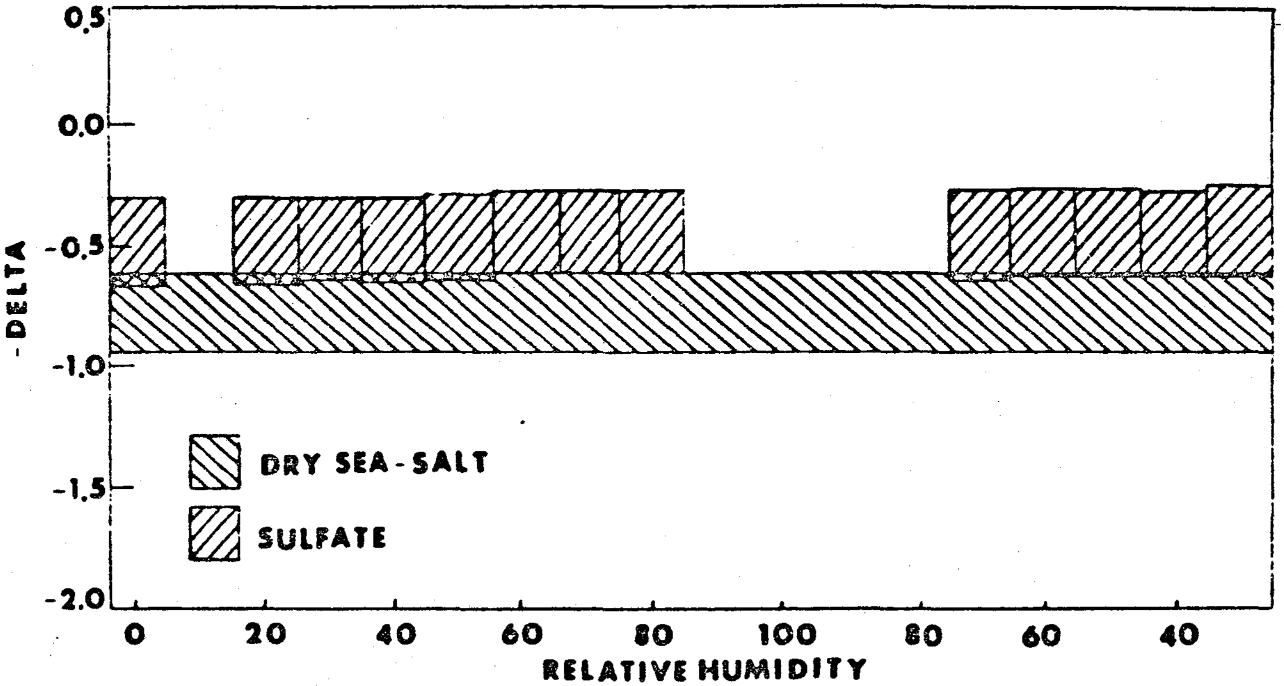

Fig. 26. Comparison of the backscatter wavelength dependence (δ) in wavelength region 3 for dry sea-salt and sulfate particles undergoing relative humidity variations. See Fig. 15.

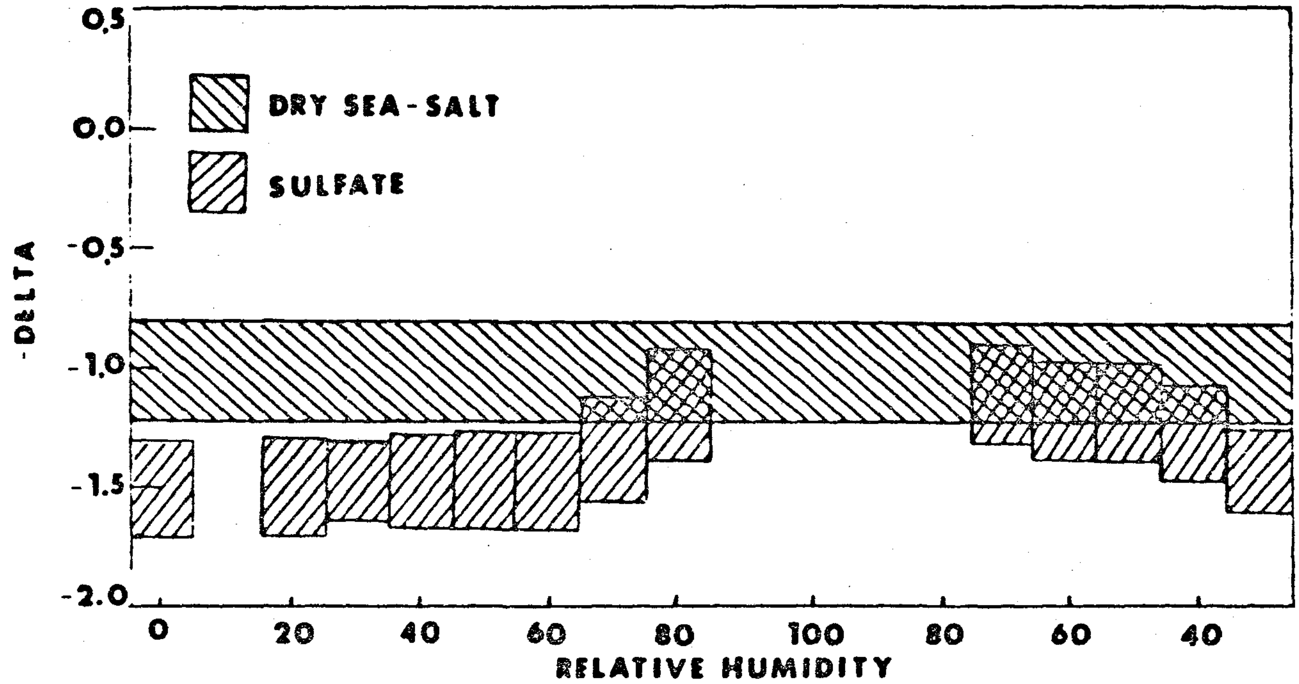

Fig. 27. Comparison of the backscatter wavelength dependence (δ) in wavelength region 4 for dry sea-salt and sulfate particles undergoing relative humidity variations. See Fig. 15.

1, 3 and 4. Once the critical relative humidity for sulfates is reached (70%), the δ values in wavelength region 4 approach those of the dry sea-salt. Figures 24 and 26 show that only wavelength regions 1 and 3 can discriminate the aerosols at 70% relative humidity. As relative humidity continues to increase to 80%, the sulfate δ values in wavelength region 1 shift towards those of the sea-salt, whereas the sea-salt δ values in wavelength region 2 shift away from the sulfate values. Figures 25 and 26 demonstrate these wavelength region shifts and show that the two aerosols can be differentiated in the wavelength regions 2 and 3.

Sulfate particles at decreasing relative humidities (from near 100%) are compared with dry sea-salt aerosols. As relative humidity decreases from 75% to 60%, δ in the wavelength region 2 can best distinguish the two aerosol compositions as shown in Figure 25. Once the relative humidity decreases to 50%, the sulfate δ values in the wavelength region 1 shift away from those of dry sea-salts shown in Figure 24. In wavelength region 2, Figure 25 shows the δ values have become more similar. At 30% relative humidity the δ values in wavelength region 4 begin to shift away from each other, thus allowing the δ discrimination.

The δ distribution in the four wavelength regions that discriminate between sea-salts and sulfates are different for decreasing relative humidities than those regions for increasing relative humidities. This difference is due to the hysteresis effect of sulfate aerosols since sulfate particles never return to their original dry size for decreasing relative humidities.

4.3 SUMMARY

Sea-salt and sulfate aerosol compositions have been characterized and identified by their theoretical backscatter wavelength dependence. Comparisons of δ for the two aerosol compositions were made at four wavelength regions for increasing and decreasing relative humidities. A summary of the results is shown in Tables 9a, 9b, and 9c. This study has shown that the influence of the natural variability of particle size distributions and relative humidity are significant. The effects of increasing and decreasing relative humidity on δ were found to be characteristic of the aerosol hysteresis curves.

Table 9a. The wavelength regions that the mean of sea-salt and sulfate aerosols at identical relative humidities are separated by the standard deviation criteria (i.e., $\sigma_{ss} + \sigma_{sf}$). The wavelength regions 1, 2, 3, and 4 are defined as 0.3-0.55, 0.55-0.9, 0.9-1.35, and 1.35-1.8 μm, respectively.

Relative Humidity	Increasing	Decreasing
0	1,4	--
20	1,4	--
30	1,4	1,4
40	1,4	--
50	1,4	2
60	4	2
70	2	2
80	2	--

Table 9b. The wavelength region that the mean of dry sulfate and sea-salt aerosols of various relative humidities are separated by the standard deviation criteria (i.e., $\sigma_{ss} + \sigma_{sf}$). The wavelength regions 1, 2, 3, and 4 are defined as 0.3-0.55, 0.55-0.9, 0.9-1.35, and 1.35-1.8 μm, respectively.

Relative Humidity	Increasing	Decreasing
0	1,4	--
20	1,4	--
30	1,4	1,4
40	1,4	1,4
50	1,4	1,4
60	1,4	4
65	4	4
70	4	4
75	--	--
80	--	--

Table 9c. The wavelength region that the mean of dry sea-salt and sulfate aerosols of various relative humidities are separated by the standard deviation criteria (i.e., $\sigma_{ss}+\sigma_{sf}$). The wavelength regions 1, 2, 3, and 4 are defined as 0.3-0.55, 0.55-0.9, 0.9-1.35, and 1.35-1.8 μm, respectively.

Relative Humidity	Increasing	Decreasing
0	1,4	--
20	1,4	--
30	1,4	1,4
40	1,4	1
50	1,4	1
60	1,3,4	2
65	1,3,4	2
70	1,3	2
75	1,3	2
80	2,3	--

V. LIDAR METHOD

A multi-wavelength lidar system provides information on the total volume backscatter coefficient as a function of wavelength. This study has theoretically shown that aerosol backscatter wavelength dependence is uniquely related to aerosol particle composition, and therefore, that multi-wavelength lidar measurements may potentially be used to infer aerosol composition. The derivation of aerosol optical properties from multi-wavelength lidar data can be difficult and inaccurate (Shipley, 1978; Klett, 1980), but under special conditions simple asymptotic solutions are available. Given simultaneous lidar returns to two wavelengths, this chapter presents a method for the computation of an average aerosol backscatter wavelength dependence.

5.1 THE DERIVATION OF

The lidar equation is given by:

$$P_\lambda R^2 = C_\lambda \sigma_{ray_\lambda}(R)\left(1 + S_\lambda(R)\right) EXP\left\{-2\tau_\lambda(R)\right\} \qquad (9)$$

where

P_λ	power returned
R	range
C_λ	lidar constant
σ_{Ray_λ}	Rayleigh scattering coefficient
λ	lidar wavelength
$S_\lambda(R) = \dfrac{\left(\dfrac{\mathbb{P}_\lambda(\pi)}{4\pi}\right)\left(\sigma_{aer_\lambda}(R)\right)}{\left(\dfrac{3}{8\pi}\right)\left(\sigma_{ray_\lambda}(R)\right)}$	Aerosol to molecular backscatter ratio
$\tau_\lambda(R) = \int_{R_0}^{R} \sigma_{aer_\lambda}(R)\,dR$	one way optical depth
$\mathbb{P}_\lambda$	normalized aerosol backscatter phase function
σ_{aer_λ}	aerosol scattering coefficient.

The lidar system constant can be eliminated by taking the ratio of the return signal at range R so that at some normalization range R_0, such that:

$$\frac{P(R)_\lambda R^2}{P(R_0)_\lambda R_0^2} = \frac{\left(1+S_\lambda(R)\right)}{\left(1+S_\lambda(R_0)\right)} \, EXP\left\{-2\left(\tau_\lambda(R)-\tau_\lambda(R_0)\right)\right\} \qquad (10)$$

Extracting volume backscatter coefficients from lidar measurements becomes problematic when optical thickness cannot be neglected. Klett (1980) discusses an analytical solution for the total scattering cross-section, given a power law relationship between total backscatter and optical thickness. This solution assumes scattering by aerosols only, and it is sensitive to any range variation of the aerosol backscatter phase function. Analytic solutions which account for scattering by aerosols and air molecules are sensitive to the magnitude of the aerosol backscattering phase function.

A simple analytic solution to the lidar equation can be obtained when lidar signals are acquired in the limit of small optical depth, such that $\tau_\lambda \simeq 0$. This limit is approximated by optically thin aerosol layers which often reside in the lower troposphere just above the mixed layer. Such layering was observed above the tropical marine mixed layer during the 1981 Global Tropospheric Experiment (Browell and Shipley, 1982). Given the additional assumption of negligible aerosol scattering at the normalization range R_0, the lidar equation may then be reduced to:

$$\lim_{\substack{S_\lambda(R)\to 0\\ \Delta T\to 0}} M_\lambda = \left(1 + S_\lambda(R)\right) \qquad (11)$$

where

$$M_\lambda = \frac{P(R)_\lambda R^2}{P(R_o)_\lambda R^2}$$

Assuming that aerosol scattering follows a power law dependence with wavelength such that:

$$\sigma_{aer_\lambda}(R) = \left(\sigma_{aer_{\lambda_o}}(R)\right)\left(\frac{\lambda}{\lambda_o}\right)^{-\alpha} \qquad (12a)$$

$$\sigma_{ray_\lambda}(R) = \left(\sigma_{ray_{\lambda_o}}(R)\right)\left(\frac{\lambda}{\lambda_o}\right)^{-4} \qquad (12b)$$

$$\frac{\mathbb{P}_\lambda(\pi)}{4\pi} = \left(\frac{\mathbb{P}_{\lambda_o}(\pi)}{4\pi}\right)\left(\frac{\lambda}{\lambda_o}\right)^{-\gamma} \qquad (12c)$$

where λ_o is a second lidar wavelength, then the scattering ratio must also follow a power law dependence. The aerosol volume backscatter coefficient is then

$$\beta_{\pi_\lambda} = \mathbb{P}_{\pi_\lambda}\,\sigma_\lambda = \beta_{\pi_{\lambda_o}}\left(\frac{\lambda}{\lambda_o}\right)^{-\delta} \qquad (12d)$$

The scattering ratio is then given by

$$S_\lambda(R) = \frac{\left(\frac{\mathbb{P}_{\lambda_0}(\pi)}{4\pi}\right)\left(\frac{\lambda}{\lambda_0}\right)^{-\gamma}\left(\sigma_{\text{aer}_{\lambda_0}}(R)\right)\left(\frac{\lambda}{\lambda_0}\right)^{-\alpha}}{\left(\frac{3}{8\pi}\right)\left(\sigma_{\text{ray}_{\lambda_0}}(R)\right)\left(\frac{\lambda}{\lambda_0}\right)^{-4}} = S_{\lambda_0}(R)\left(\frac{\lambda}{\lambda_0}\right)^{4-\delta} \tag{13}$$

where $\delta = \alpha + \gamma$. Given negligible optical depth and no aerosol scattering at the normalization range R_0, the wavelength dependence for backscatter can be obtained directly from lidar measurements at two wavelengths, such that:

$$\hat{\delta} = 4 - \frac{\ln\left(\frac{M_\lambda - 1}{M_{\lambda_0} - 1}\right)}{\ln\left(\frac{\lambda}{\lambda_0}\right)} \tag{14a}$$

where $\hat{\delta}$ denotes a lidar-derived estimate of the true value $\tilde{\delta}$.

5.2 ERROR ANALYSIS

Systematic errors in $\hat{\delta}$ which arise due to the assumptions of negligible optical depth and no aerosol backscatter in the "clean" region at range R_0 are now discussed. The effects of both assumptions on the lidar inferred value $\hat{\delta}$ are computed for $\tilde{\delta} = 2.0$ and $\tilde{\delta} = 0.5$ given lidar wavelengths at 300 nm and 600 nm. The sensitivity of these systematic errors to the aerosol scattering ratio is also examined.

To estimate the deviation of $\hat{\delta}$ (the lidar-derived value) from $\tilde{\delta}$ (the true value) as aerosol optical depth increases but with no aerosol backscatter at range R_0, Eq. 14 is expanded to:

$$\hat{\delta} - \tilde{\delta} = (4 - \tilde{\delta}) - (w) \left\{ \ln \frac{\left(1 + S_\lambda(R) f\right) e^{(-2\Delta\tau g)} - 1}{\left(1 + S_\lambda(R)\right) e^{(-2\Delta\tau)} - 1} \right\} \qquad (15)$$

where

$$w = \left\{ \ln\left(\frac{\lambda}{\lambda_0}\right) \right\}^{-1}$$

$f = \left(\frac{\lambda}{\lambda_0}\right)^{4-\delta}$ backscatter factor

$g = \left(\frac{\lambda}{\lambda_0}\right)^{-\alpha}$ extinction factor

Given the assumption of small optical depth such that $\Delta\tau_\lambda \ll 1$, Eq. 15 can be approximated by:

$$\hat{\delta} - \tilde{\delta} \simeq (4-\tilde{\delta}) - (w)\left\{\ln\left(1-2\Delta\tau\cdot g\left(\frac{1}{S_\lambda(R)f}\right)\right)\right. \tag{16}$$

$$\left. -\ln\left(1-2\Delta\tau\left(1-\frac{1}{S_\lambda(R)}\right)\right) + \ln f\right\}$$

If the scattering ratio is large (i.e., $S_\lambda(R) >> 0$), then the logarithmic terms in Eq. 16 can be approximated by:

$$\ln\left\{1-2\Delta\tau\cdot g\left(1+\frac{1}{S_\lambda(R)f}\right)\right\} \approx -2\Delta\tau\cdot g \tag{17a}$$

and

$$\ln\left\{1-2\Delta\tau\left(1+\frac{1}{S_\lambda(R)}\right)\right\} \approx -2\Delta\tau \tag{17b}$$

such that

$$\hat{\delta} - \tilde{\delta} \simeq (4-\tilde{\delta}) - (w)\left\{-2\Delta\tau(g-1) + \ln f\right\} \tag{18}$$

Equation 18 shows that the systematic variation in $\hat{\delta}$ due to finite optical depth is independent of $S_\lambda(R)$ for large scattering ratios. This independence is demonstrated in Fig. 28, where the systematic variation of

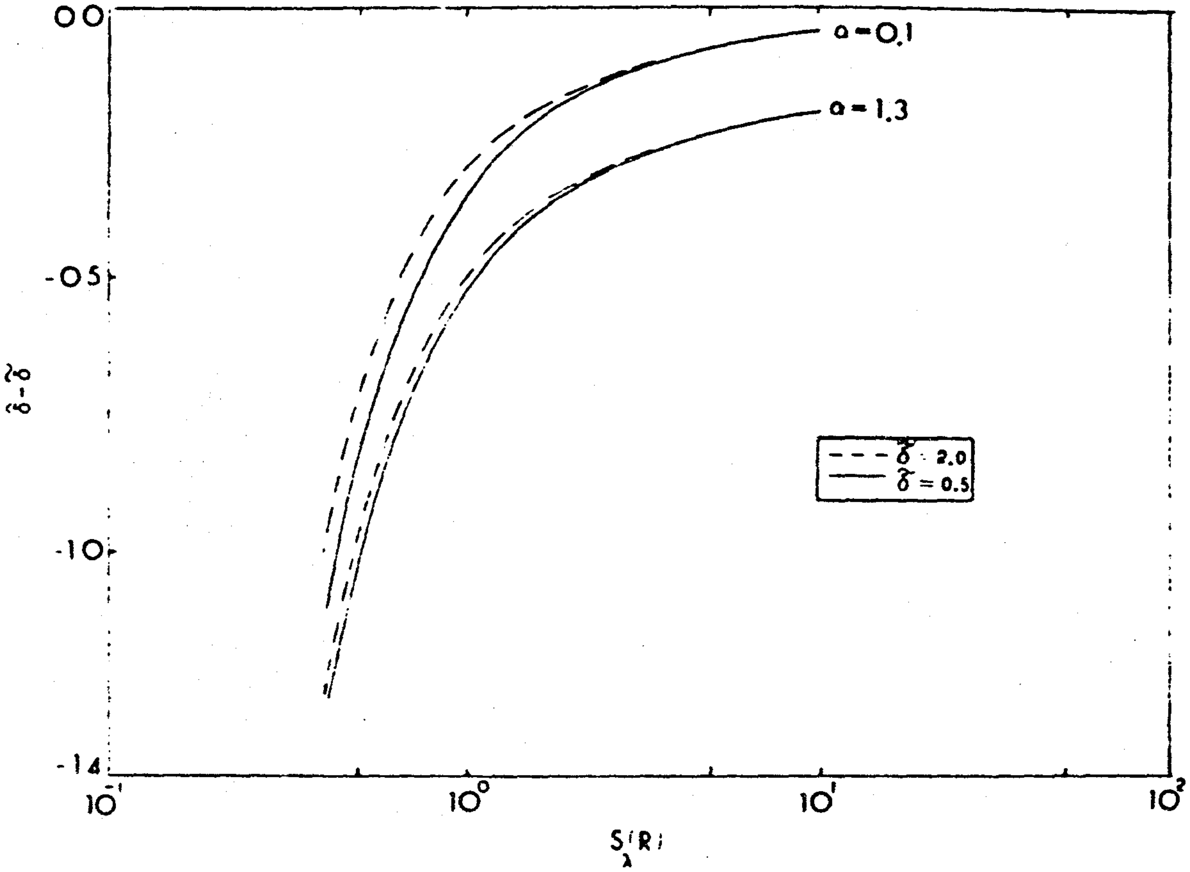

Fig. 28. The systematic variation of $\hat{\delta} - \tilde{\delta}$ due to an optical depth of 0.1 as a function of the scattering ratio, assuming no aerosol scattering at the normalization range R_o.

$(\hat{\delta} - \tilde{\delta})$ for $\tilde{\delta} = 0.5, 2.0$ is shown as a function of $S_\lambda(R)$ with $\Delta\tau = 0.1$ and $\alpha = 0.1, 1.3$. For small $S_\lambda(R)$, $\hat{\delta}$ is shown to be very sensitive to the wavelength dependence of optical depth, and $\hat{\delta}$ underestimates $\tilde{\delta}$.

The systematic variation of $\hat{\delta}$ from $\tilde{\delta}$ as the scattering ratio at range R_0 becomes significant and is given by:

$$\hat{\delta} - \tilde{\delta} = (4 - \tilde{\delta}) - (w)\left\{\ln\left(\frac{1 + fS_\lambda(R)}{1 + fS_\lambda(R_0)} - 1\right) - \ln\left(\frac{1 + S_\lambda(R)}{1 + S_\lambda(R_0)} - 1\right)\right\} \tag{19}$$

where $\Delta\tau$ is assumed to be negligible. Letting $S_\lambda(R) = S_\lambda(R_0) + A$, the normalized backscatter terms in the Equation can be expressed as:

$$\frac{1 + fS_\lambda(R)}{1 + fS_\lambda(R_0)} - 1 = \frac{fA}{1 + fS_\lambda(R_0)}$$

and Equation 19 is transformed to:

$$\hat{\delta} - \tilde{\delta} = (4 - \tilde{\delta}) - (w)\left\{\ln\left(\frac{f(1 + S_\lambda(R_0))}{1 + fS_\lambda(R_0)}\right)\right\} \tag{20}$$

Equation 20 shows that the systematic variation of $\hat{\delta}-\tilde{\delta}$ associated with $S_\lambda(R_0)$ has no dependence on $S_\lambda(R)$ when $\Delta\tau = 0$. Fig. 29 shows that $\hat{\delta}$ overestimates $\tilde{\delta}$ when significant backscatter is encountered at the "clean" normalization range R_0.

5.3 THIN AEROSOL LAYER

The NASA-Langley UV-DIAL system (Browell, et al., 1983), was operated over the state of Ohio as part of the 1980 Persistent Elevated Pollution Episode Northeast Regional Oxidant Study (PEPE/NEROS). Lidar measurements were obtained at two wavelengths to create horizontal cross-sections of aerosol spatial distributions under the flight path of the lidar instrument. During a flight on July 24, 1980, a thin aerosol layer was encountered above the continental mixed layer as shown in Figs. 30a and 30b. In these figures, the lidar backscatter data is presented in gray scale where darker shading represents more aerosol backscattering.

The thin aerosol layer located at 2700 m (AGL) and first encountered at 40° 02'N, 82° 48'W is shown emanating from deeper convection upwind. In situ measurements were made in the vicinity of these cross-sections, but positive identification of the aerosols in this layer was not made. Yet, the layer is associated with cumulus cloud activity at this altitude from 39° 02'N, 84° 39'W to approximately

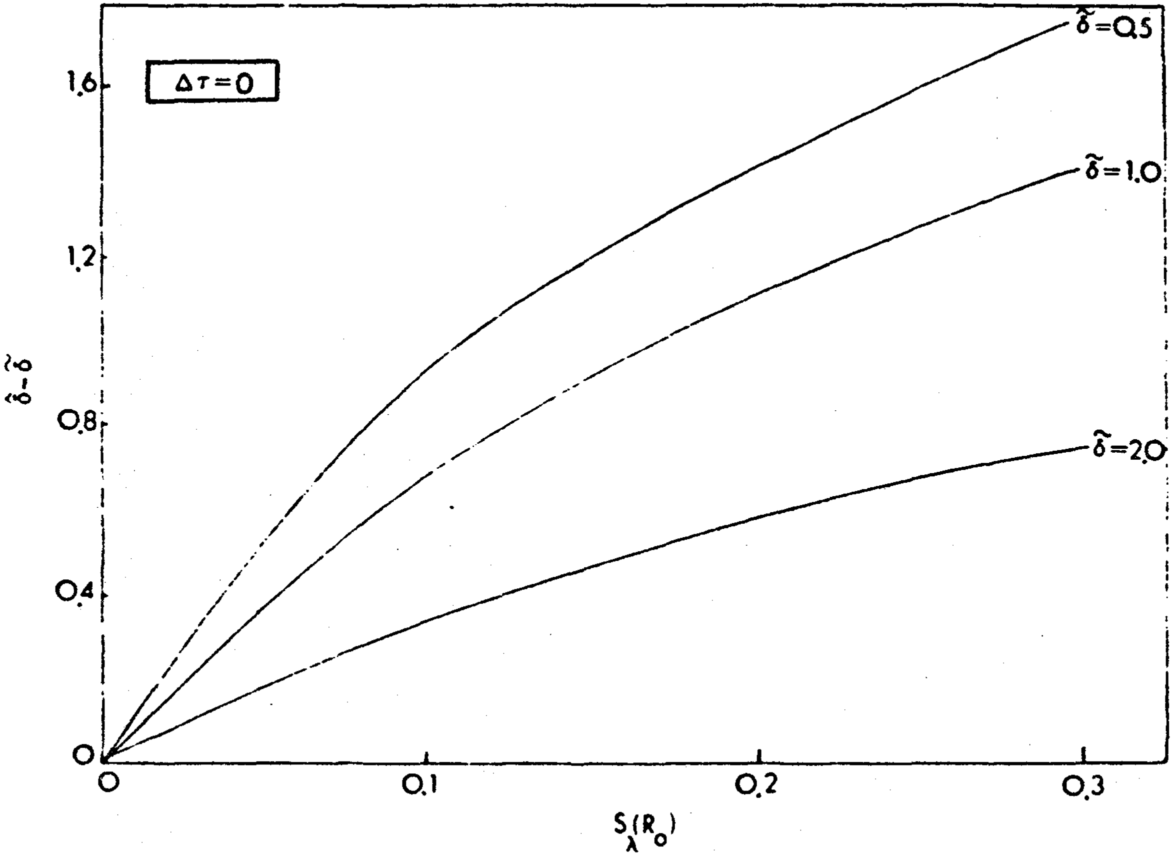

Fig. 29. The systematic variation in $\hat{\delta}-\tilde{\delta}$ as scattering at range R_o increases, assuming no optical depth.

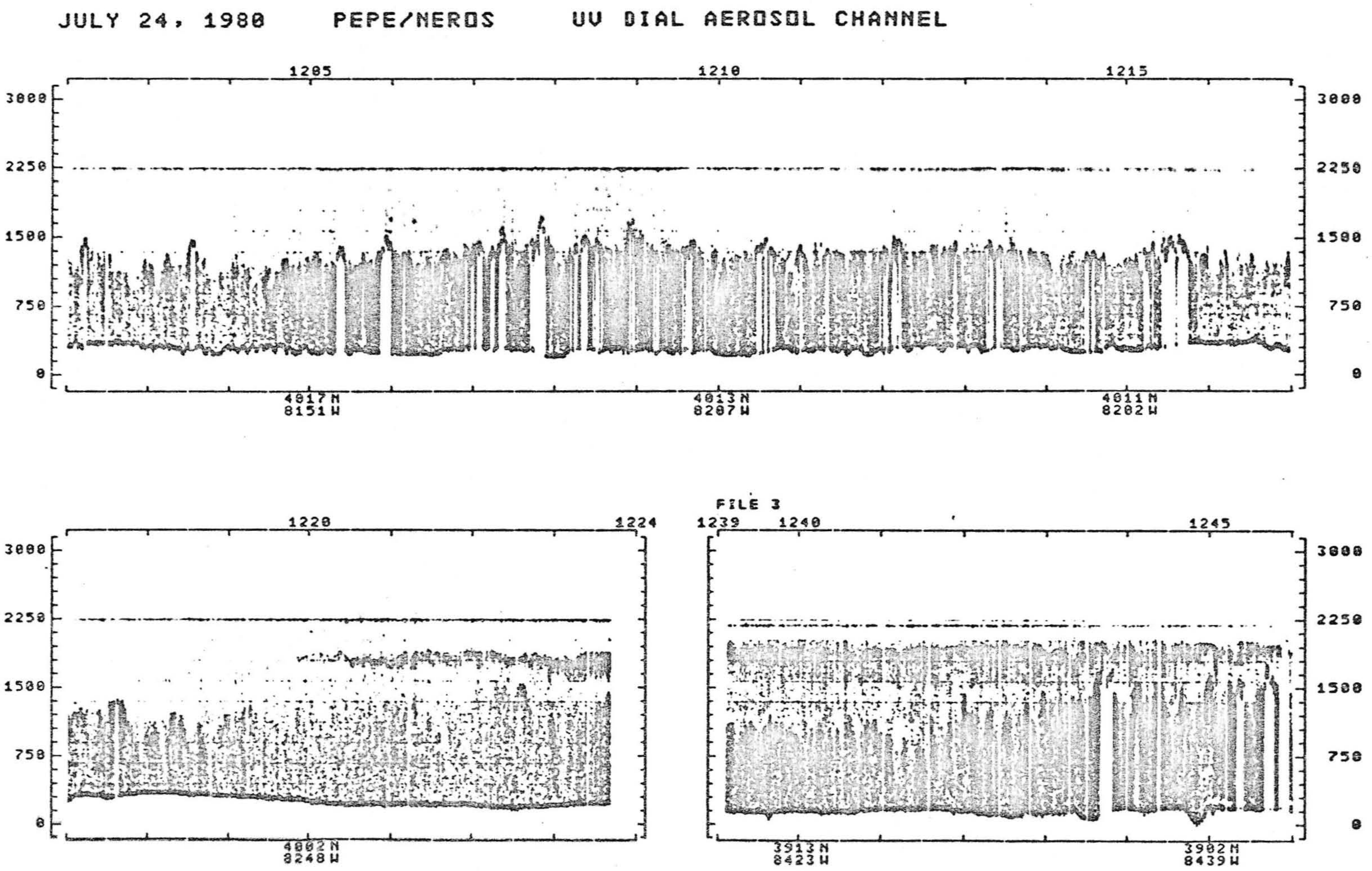

Fig. 30a. Time (EDT) - height (meters) lidar aerosol cross-sections. Darker shading represents higher aerosol concentrations.

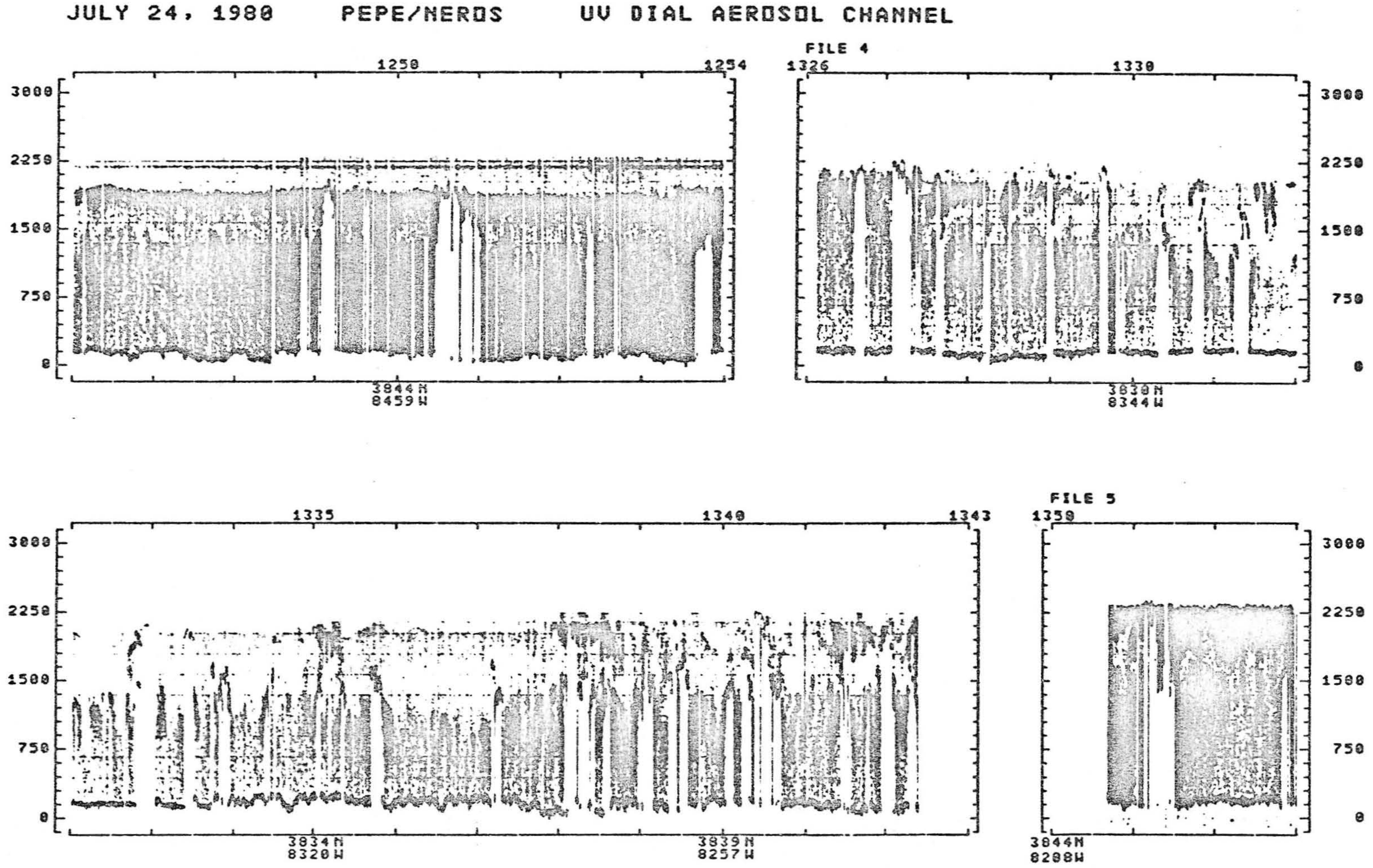

Fig. 30b. Time (EDT) - height (meters) lidar aerosol cross-sections. Darker shading represents higher aerosol concentrations.

38° 44'N, 84° 59'W, where mixed layer aerosols are being released into the free troposphere. Thus, the thin aerosol layer appears to have originated from continental sources. A relative humidity of 65% was computed for the aerosol layer from in situ temperature and dew point measurements made in the vicinity over Dayton, Ohio.

The raw DIAL signal profiles at the wavelengths 300 and 600 nm are shown in Figs. 31 and 32, respectively. The signals are shown after background has been subtracted and a range squared attenuation correction has been applied. The ordinate represents range (or decreasing altitude) in increments of 150 m. $\hat{\delta}$ was computed throughout the layer from range 1400 m to 1700 m with R_0 equal to 1400 m under the assumptions of no scattering at R_0 and negligible optical depth. Values for $\hat{\delta}$ averaged 0.61±0.21 throughout the thin aerosol layer. The backscatter wavelength dependence of sulfate and sea-salt aerosols were compared for increasing and decreasing relative humidities in Chapter IV. As shown in Fig. 15, the true aerosol classes are not totally distinguishable within the one standard deviation criterion at 60 and 70% relative humidity. However, the spread in δ values calculated theoretically for sulfate aerosols is approximately the same as that determined empirically in the thin aerosol layer. Although this agreement does not prove that the aerosol layer is composed of sulfate particles, it does

ORIGINAL PAGE IS
OF POOR QUALITY

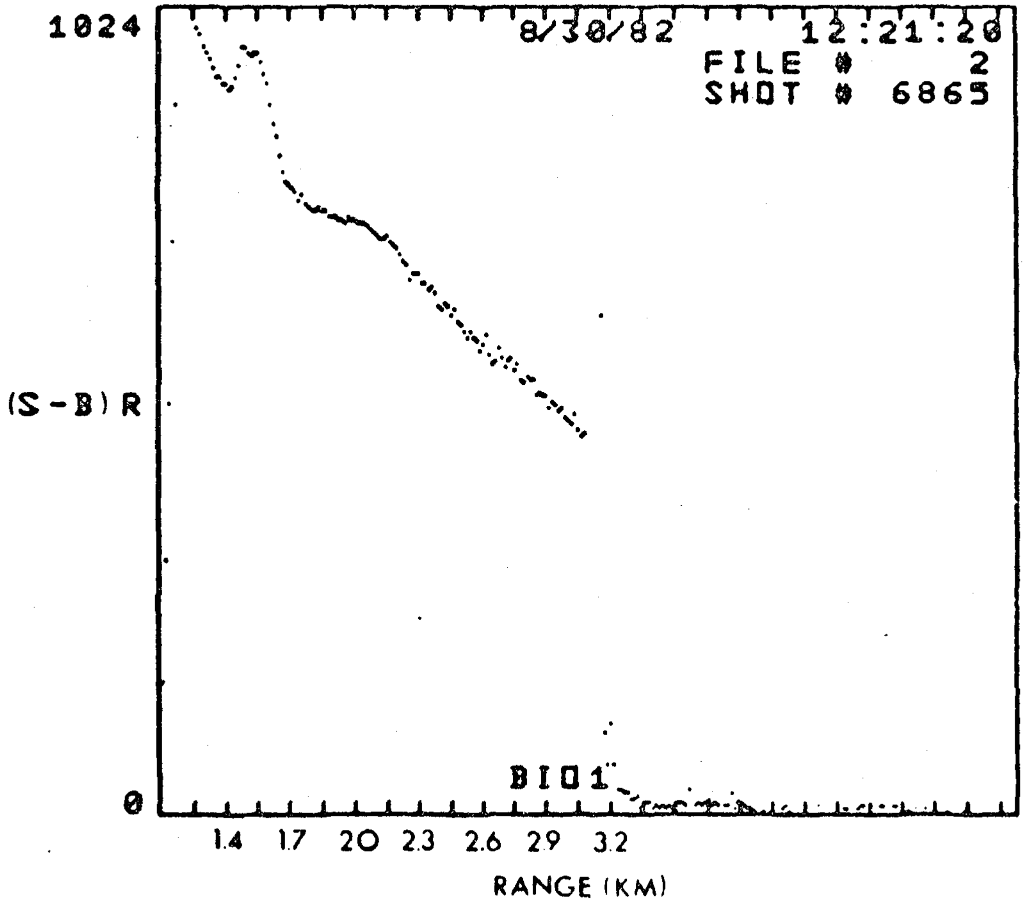

Fig. 31. Raw DIAL signal profile corrected for range squared attenuation at wavelength 300 NM (BI01). The signals minus signal background are presented as a function of range R.

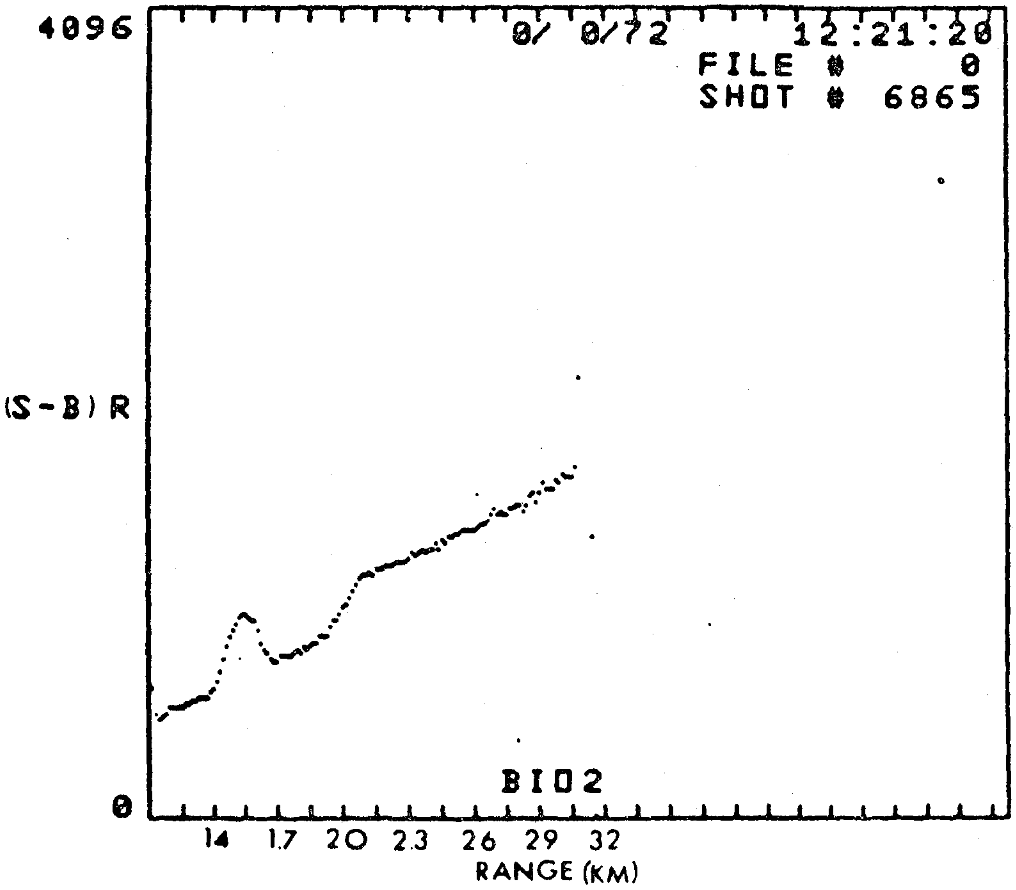

Fig. 32. Raw DIAL signal profile corrected for range squared attenuation at wavelength 600 NM (BI02). The signals minus signal backgrounds are presented as a function of range R.

indicate that it is not dominated by sea-salt aerosols.

VI. CONCLUSIONS

This thesis examined the wavelength dependence of volume backscatter for two tropospheric aerosol classes; namely, sea-salts and sulfates. Model calculations have shown that these two key aerosol classes can be characterized and identified by their backscatter wavelength dependence. Also, it was found that the natural variability of aerosol physical properties such as particle size distributions, refractive index, and relative humidity had a considerable effect on backscatter wavelength dependence. The model results show that a multi-wavelength lidar system may be able to identify the composition of aerosol layers by their backscatter wavelength dependence at visible and near IR wavelengths.

The backscatter wavelength dependence of sea-salt and sulfate particles was computed for twenty-five log normal particle size distributions at seventeen increasing and decreasing relative humidities. The variation in the backscatter wavelength dependence exponent, δ , for both sea-salt and sulfate aerosol compositions was found to be a function of the characteristic hysteresis curves of the aerosols. For decreasing relative humidities, it was shown that the δ values for the sulfate aerosol never returns to those for the original dry distributions; whereas, the sea-salt δ values do return to values characteristic of the dry state.

A simple method to retrieve δ from a two wavelength lidar system was derived for the special conditions of small optical depth and no scattering at the normalization range R_o. Such conditions are encountered often in the free troposphere. An error analysis of these assumptions revealed that δ is not sensitive to optical depth at large values of the scattering ratio $S_\lambda(R)$. This was not the case for small scattering ratios however. For the assumption of no scattering at the normalization range R_o, small δ values were found to be grossly overestimated as $S_\lambda(R_o)$ increased from zero. This overestimation decreases in importance as δ becomes large.

Estimates of δ were computed throughout a thin aerosol layer for lidar profiles at two wavelengths. The composition of the layer appeared to be of continental origin with a relative humidity of 65%. A mean and first standard deviation of δ for the aerosol layer was compared with the 65% increasing and decreasing relative humidity model case, and found to be approximately the same. Although this comparison does not prove that the composition of the layer is sulfate, it does suggest that very little or no sea-salt particles are present.

This study has shown that a multi-wavelength lidar does have the potential to characterize broad classes of aerosol compositions. The optical properties of sea-salt and sulfate aerosol compositions have been shown to be uniquely related to backscatter wavelength dependence under many physical situations. The characterization of thin aerosol layer composition by a two wavelength lidar was explored and appears possible. Problems can arise when aerosol layers become optically thick or when suitably "clean" regions for lidar signal calibration are not available. Under these situations, an analytical procedure can be used to obtain backscatter wavelength dependence. The analytical inversion of lidar signals for information on the backscatter or total extinction coefficient profile requires additional information on aerosol optical properties at some calibration range R_o (Klett, 1980), or an average value over a range interval, $R_1 < R < R_2$ (Shipley, 1978). This information can be obtained using the average slope method in the mixed layer, or by an independent measurement of total optical depth by passive techniques (Norten et al, 1980).

REFERENCES

Blanchard, D. L., and A. H. Woodcock. 1980: The production concentration and vertical distribution of the sea-salt aerosol. Annals New York Academy of Science, pp. 330-347.

Browell, E. V., and S. T. Shipley. 1982: Airborne lidar investigation of ozone and aerosols in the non-urban troposphere. Proceedings of the Second Stymposium on the Nonurban Troposphere, Williamsburg, Virginia, May 25-28, 1982.

Browell, E. V., A. F. Carter, S. T. Shipley, R. J. Allen, C. F. Butler, M. N. Mayo, J. H. Siviter Jr., and W. M. Hall. 1983: NASA multipurpose airborne DIAL system and measurements of ozone and aerosol profiles. J. Appl. Opt., 22, 522-534.

Bryant, H. C., and A. J. Cox. 1966: Mie Theory and the glory. J. Opt. Soc. Am., 56, 1529-1532.

Covert, D. S., R. J. Charlson, and N. C. Ahlquist. 1972: A study of the relationship of chemical composition and humidity to light scattering by aerosols. J. Appl. Meteor., 11, 968-976.

Deirmendjian, D. 1969: Electromagnetic scattering on spherical polydispersions, American Elsevier, New York.

Fitzgerald, J. W. 1975: Approximation formulas for the equilibrium size of an aerosol particle as a function of its dry size and composition and the ambient relative humidity. J. Appl. Meteor., 14, 1044-1049.

Fitzgerald, J. W., W. A. Hoppel, and M. A. Vietti. 1982: The size and scattering coefficient of urban aerosol particles at Washington, D.C. as a function of relative humidity. J. Atmos. Sci., 39, 1838-1852.

Hale, G. M., and M. R. Querry. 1973: Optical constants of water in the 200nm to 200 m wavelength region. J. Appl. Opt., 12, 555-563.

Hanel, G. 1968: The real part of the mean complex refractive index and the mean density of samples of atmospheric aerosol particles. Tellus, 20, 371-379.

________. 1972: Computations of the extinction of visible radiation by atmospheric aerosol particles as a function of the relative humidity, based upon measured properties. Aerosol Sci., 3, 377-386.

________. 1970: The size of atmospheric aerosol particles as a function of the relative humidity. Beitr. Phys. Atmos., 43, 119-132.

________. 1971: New results concerning the dependence of visibility on relativity and their significance in a model for visibility forecast. Beitr. Phys. Atmos., 44, 137-167.

________. 1976: The properties of atmospheric aerosol particles as functions of relative humidity at thermodynamic equilibrium with the surrounding moist air. Advances in Geophysics, 19, 73-88.

Hanel, G., and B. Zarkl. 1979: Aerosol size and relative humidity: Water uptake by mixtures of salts. Tellus, 31, 478-486.

Hanel, G., and M. Lehman. 1980: Equilibrium size of aerosol particles and relative humidity: New experimental data from various aerosol types and their treatment for cloud physics applications. Contrib. Atmos. Phys., 54, 57-71.

Herbert, F. 1975: A reexamination of the equilibrium conditions in the theory of water drop nucleation. Tellus, 27, 406-413.

Junge, C. 1953: Die rolle der aerosol and der gasformigen Beimengangen der luft im spurensloffhaushatt der troposphare. Tellus, 5, 1-26.

Junge, C., E. Roberson, and F. L. Ludwig. 1969: A study of aerosols in pacific air masses. J. Appl. Meteor., 8, 340-347.

Kelkar, D. N., and P. V. Joshi. 1977: A note on the size distribution of aerosols in urban atmospheres. Atmos. Environ., 2, 531-534.

Kerker, M. 1969: The scattering of light. Academic Press, New York, 666 pp.

Klett, James D. 1980: Stable analytical inversion solution for processing lidar returns. J. Appl. Opt., 20, 211-220.

Metnicks, A. 1958: The size spectrum of large and giant sea-salt nuclei under maritime conditions. Geophys. Bull. School of Cosmic Phys. Dublin. 15, 1-50.

Meszaros, A. 1971: On the variation of the size distribution of large and giant atmospheric particles as a function of relative humidity. Tellus, 23, 436-440.

Meszaros, A., and K. Vissy. 1974: Concentration, size distribution, and chemical nature of atmospheric aerosol particles in remote oceanic areas. Aerosol Sci., 5, 101-109.

Meszaros, A. 1978: On the concentration and size distribution of atmospheric sulfate particles under rural conditions. Atmos. Environ., 12, 2425-2428.

Mudd, H. T., C. H. Kruger, and E. R. Murray. 1982: Measurement of IR laser backscatter spectra from sulfuric acid and ammonium sulfate aerosols. Appl. Opt., 21, 1146-1154.

Mugnai and Wiscombe. 1980: Scattering of radiation by moderately nonspherical particles. J. Atmos. Sci., 37, 1291-1307.

Norton, C. C., F. R. Mosher, B. Hinton, D. W. Mortin, D. Santek and W. Kuhlo. 1980: A model for calculating desert aerosol turbidity over the oceans for geostationary satellite data. J. Appl. Met., 18, 633.

Nussenzvieg, H. M. 1969: High-frequency scattering by a transparent sphere. II. Theory of the rainbow and the glory. J. Math. Phys., 10, 125-176.

Orr, C., F. K. Hurd, and W. J. Corbett. 1958: Aerosol size and relative humidity. J. Colloid Sci., 13, 472-482.

Paltridge, G. W., and C. M. R. Platt. 1976: Radiative processes in Meteorology and Climatology, Elasvier Scientific Publishing Company, Amsterdam.

Patterson, E. M., C. S. Kiang, A. C. Delany, A. F. Wortbury, A. C. Leslie, and B. J. Huebert. 1980: Global measurements of aerosols in Remote continental and maritime regions: concentrations, size distributions, and optical properties. J. Geophys. Res., 85, 7361-7376.

Russell, P. B., B. M. Morley, J. M. Livingston, G. W. Grams, and E. M. Patterson. 1981: Improved simulation of aerosol, clouds and density measurements by shuttle lidar. NASA Tech. Mem. 16052, NASA Langley Research Center, Hampton, Virginia.

Shettle, E., and R. W. Fenh. 1979: Models for the aerosols of the lower atmosphere and the effects of humidity variations on their optical properties. AFGL-TR-79-0214, Hanscom AFB, MA, 01731.

Shipley, S. T., and J. A. Weinman. 1978: A numerical study of scattering by large dielectric spheres. J. Opt. Soc. Am., 68, 130-134.

Shipley, S. T. 1978: The measurement of rainfall by lidar. Ph.D. dissertation, University of Wisconsin, Madison.

Tang, I. N. 1976: Phase transofrmation and growth of aerosol particles composed of mixed salts. J. Aerosol Sci., 7, 361-371.

Tang, I. N., H. R. Munkelwitz, and J. G. Davies. 1977: Aerosol growth Studies II: Preparation and growth measurements of monodisperse salt solutions. J. Aerosol Sci., 8, 149-159.

Tang, I. N., H. Munkelwitz. 1977: Aerosol growth studies III: Ammonium bisulfate aerosols in a moist atmosphere. J. Aerosol Sci., 8, 321-330.

Tang, I. N., H. R. Munkelwitz, and J. G. Ravies. 1978: Aerosol growth studies IV: Phase transformation of mixed salt in a moist atmosphere. J. Aerosol Sci., 9, 505-511.

Thomalla, E., and H. Quenzel. 1982: Information content of aerosol optical properties with respect to their size distribution. Appl. Opt., 21, 3170-3177.

Thudium, J. 1978: Water uptake and equilibrium sizes of aerosol particles at high relative humidities: Their dependence on the composition of the water soluble material. PAGEOPH, 116, 130-148.

Van de Hulst. 1957: Light scattering by small particles. John Wiley and Sons Inc., New York, 470 pp.

Volz, F. E. 1972: Infrared refractive index of atmospheric aerosol substances. J. Appl. Opt., 11, 755-759.

__________. 1973: Infrared optical constants of ammonium sulfate, Sahara dust, volcanic pumice, and fly ash. J. Appl. Opt., 12, 564-567.

Whitley, K. T., R. B. Huson, and B. Y. Liu. 1972: The aerosol size distribution of Los Angeles Smog. J. Colloid Interface Sci., 39, 177-204.

Whitley, K. T., and B. Cantrell. 1975: Atmospheric aerosols -- characteristics and measurements. Presented at the International Conference on Environmental Sensing and Assessment, September 19-22, 1976, Las Vegas, Nevada.

Willeke, K., K. T. Whitby, W. Clark, and V. A. Marple. 1974: Size distributions of Renver aerosols -- a comparison of two sites. Atmos. Environ., 8, 609-633.

Willeke, K., and K. T. Whitby. 1975: Atmospheric aerosols. Size distribution interpretation. J. Air Poll. Control Assoc., 25, 529-534.

Winkler, P., and C. Junge. 1972: The growth of atmospheric aerosol particle as a function of relative humidity. Part I. Method and measurements at different locations. J. Rech. Atm., 617-638.

Wiscombe, W. 1979: Mie scattering calculations: Advances in techniques and fast, vector-speed computer code. NCAR/TN-140-STR. National Center for Atmospheric Research, Boulder, Colorado.

Wright, M. L. 1980: Lidar determination of the composition of atmospheric aerosols. NASA-CR-152355. SRI International Corp., Menlo Park, California.

END

DATE

FILMED

SEP 27 1984